Michigan State University

National Superconducting Cyclotron Laboratory

(^{12}C,^{12}B) AND (^{12}C,^{12}N) REACTIONS AT E/A = 70 MeV AS SPIN PROBES: CALIBRATION AND APPLICATION TO 1^+ STATES IN ^{56}Mn

N. ANANTARAMAN, J.S. WINFIELD, SAM M. AUSTIN, J.A. CARR, C. DJALALI, A. GILLIBERT, W. MITTIG, J.A. NOLEN, Jr., and ZHAN WEN LONG

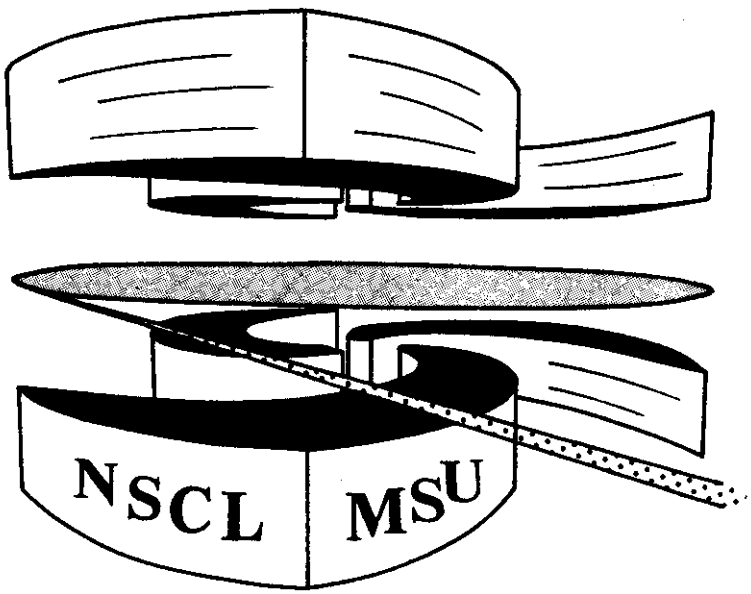

MSUCL-756

FEBRUARY 1991

MSUCL-756
February, 1991

(^{12}C, ^{12}B) and (^{12}C, ^{12}N) reactiona at E/A = 70 MeV as spin probes: calibration and application to 1^+ states in ^{56}Mn

N. Anantaraman,[1] J.S. Winfield,[1] Sam M. Austin,[1,2] J.A. Carr,[3]
C. Djalali,[1,a] A. Gillibert,[4,b] W. Mittig,[4]
J.A. Nolen, Jr.,[1,2] and Zhan Wen Long[4,c]

[1]National Superconducting Cyclotron Laboratory,
Michigan State University, East Lansing, Michigan 48824-1321

[2]Department of Physics and Astronomy
Michigan State University, East Lansing, Michigan 48824-1116

[3]Supercomputer Computations Research Instititute,
Florida State University, Tallahassee, Florida 32306-4052

[4]CANIL, B.P. 5027, 14021 Caen Cedex, France

Submitted to Phys. Rev. C on February 4, 1991.

Abstract: Angular distributions have been measured for $0^+ \rightarrow 1^+$ transitions with the (^{12}C, ^{12}B) reaction on targets of ^{12}C, ^{26}Mg, ^{54}Fe, ^{58}Ni, and ^{90}Zr and with the (^{12}C, ^{12}N) reaction on targets of ^{12}C and ^{56}Fe. The bombarding energy was E/A = 70 MeV, and small-angle data were obtained. A comparison of the cross sections measured for the (^{12}C, ^{12}B) reaction with the results of Distorted Wave Approximation calculations indicates that $0^+ \rightarrow 1^+$ transitions are predominantly one-step at E/A = 70 MeV. The calculated cross sections are generally in good agreement (to within 40% in magnitude) with the measured cross sections, and the angular distributions are well described quantitatively in many cases. A correlation between cross sections and known Gamow-Teller (GT) strengths B(GT) for the corresponding transitions has been found. This correlation, which is weakly dependent on the target mass, establishes a calibration for the reactions. It is used to determine B(GT) values of astrophysical interest for two low-lying 1^+ levels in ^{56}Mn from the cross sections measured for the $^{56}Fe(^{12}C, ^{12}N)^{56}Mn$ reaction. The results are compared with two shell-model calculations performed to obtain B(GT) for $^{56}Fe \rightarrow ^{56}Mn$ transitions and with another calculation from the literature. Computational tests were performed to evaluate (a) the contribution to the cross sections of terms not present in nucleon-induced charge exchange reactions and (b) the extent to which the cross sections provide a measure of GT strength.

PACS numbers : 25.70.Cd, 24.50.+g, 97.10.Cv

I. INTRODUCTION

In the past decade it has been shown that, at sufficiently high energies, $E \geq 100$ MeV, the (p,n) and (n,p) charge-exchange reactions are strongly dominated by the spin-isospin force and can be used as a probe of isovector spin strength in nuclei.[1-4] In particular, these reactions, at small momentum transfer, provide a reasonable measure of Gamow-Teller (GT) strength. Yet much remains to be done in the study of collective nuclear spin-isospin vibrations. Little is known about the behavior of the higher multipole resonances. The isovector spin monopole resonance has not been located. It is also necessary to know electron capture strengths, which are directly related to GT β^+ strengths, for nuclei in the upper sd shell and in the Fe region in order to understand the evolution of type II supernovae and nucleosynthesis in supernova explosions.[5] The (n,p) reaction has been used to explore β^+ strength but it has the drawback of having marginal resolution (typically 1 MeV) for spectroscopic studies.[3,6]

In principle, heavy-ion charge-exchange reactions, for example (^{6}Li,^{6}He), (^{12}C,^{12}N), or (^{12}C,^{12}B), offer significant advantages for such studies, in that the quantum numbers of the states involved can be chosen to limit the transitions strictly to $\Delta S = \Delta T = 1$, thus giving cleaner spectra. In addition, both the initial and final states involve charged particles, so that better resolution is often possible. The use of heavy-ion charge-exchange reactions involves, however, complexities that are not present for high-energy (p,n) and (n,p) reactions.

First among these issues is that the reactions must be dominated by the one-step process if the selection rules noted above are to hold and if there is to be a close correlation between the observed cross section and isovector spin strength. Since successive transfer reactions dominate the cross section at low energies, relatively high bombarding energies must be used. It has been established experimentally that at energies above about 25 MeV/nucleon, the (^{6}Li,^{6}He) reaction is one-step in nature and can be used for measuring GT strength.[7-9] In the case of the (^{12}C,^{12}N) reaction, it was shown[10] that the one-step mechanism should be dominant above about 50 MeV/nucleon for $0^+ \rightarrow 1^+$ transitions. Experimental data[10,11] and detailed calculations[12] both support this conclusion.

A second issue is that of the strong absorption in heavy-ion reactions; only the surface region of the projectile and target transitions densities is sampled in the reaction. As a consequence, one expects that the reaction is sensitive to a large range of the momentum transfer q in the transition density. This will make the cross section for the reaction a poor measure of Gamow-Teller strength, which is equal to the value of the corresponding transition density at $q \approx 0$, unless all transition densities have the same q dependence. Unfortunately, this is not the case. However, as discussed in this paper, Distorted Wave Approximation (DWA) calculations for a variety of transitions in $^{26}Mg(^{12}C, ^{12}B)^{26}Al$ show, surprisingly, that the cross section is rather closely proportional to the GT strength for these transitions. This is in spite of the fact that the transition densities involved have rather different q dependences. A theoretical investigation of this question has given us some insight into the reasons for this behavior.[13]

In the present paper we take a different point of view by addressing phenomenologically the question of the suitability of heavy-ion charge-exchange reactions for the measurement of GT strengths. Following the approach of the (p,n) work,[1,2] we attempt to establish an empirical calibration curve for $\hat{\sigma}$, the cross section per unit GT strength B(GT), as a function of target mass, by studying a variety of $(^{12}C, ^{12}B)$ transitions whose B(GT) values are known. If a consistent result is obtained, then one can use this curve to determine B(GT) from a measured charge-exchange cross section. The scatter of the calibration measurements about the curve provides a measure of the accuracy of the procedure.

A third issue related to heavy-ion charge-exchange reactions is that the internal structure of the projectile allows additional amplitudes, not all proportional to GT strength, to contribute to the cross section. Computational tests have been performed to evaluate the importance of such amplitudes. The amplitudes were found to be small.

We have measured cross sections for the $(^{12}C, ^{12}B)$ and $(^{12}C, ^{12}N)$ reactions on a variety of nuclei at a laboratory bombarding energy of 70 MeV/nucleon. An emphasis was placed on obtaining measurements at small angles, including 0°. The $(^{12}C, ^{12}B)$ results on ^{12}C, ^{26}Mg, ^{54}Fe, ^{58}Ni,

and ^{90}Zr are used to establish a calibration curve as discussed above. This calibration curve and a measurement of the cross section for the $^{56}Fe(^{12}C, ^{12}N)$ reaction are used to obtain the GT strength of known 1^+ states in ^{56}Mn. These results are compared with two shell-model calculations which we have performed and with another calculation[14] which has been used to provide the electron capture strength needed in predictions of supernova evolution and collapse.

II. EXPERIMENTAL PROCEDURE

Self-supporting targets, of thickness about 1 mg/cm^2 (except for ^{12}C, which had 0.48 mg/cm^2 thickness), were bombarded by an E_{lab}/A = 70 MeV ^{12}C beam from the GANIL coupled cyclotrons. The outgoing particles were analyzed by the magnetic spectrometer SPEG.[15] Momentum and scattering angle information was obtained by reconstruction of trajectories at the focal plane. The focal plane detector consisted of two position-sensitive multiwire drift chambers, an ionization chamber and a stopping plastic scintillator. The gas counters were filled with isobutane gas. The drift chambers provided two x-y measurements, one on each side of the focal plane. Pile-up events in the drift chambers were rejected by a software requirement that the time signals from both ends of the delay lines add up to a constant (the length of the wire). This was a significant correction for the second counter when the detected ions were ^{12}B, since the overall count rate was much higher in this case than for ^{12}N. Since the experiment was intended as a survey-type measurement, it was not possible to obtain good statistics for most of the spectra.

The aperture of the spectrometer covered -0.5° to +3.5° in the horizontal reaction plane for the ($^{12}C, ^{12}N$) reaction. For the ($^{12}C, ^{12}B$) reaction, although the spectrometer aperture covered -3.7° to +0.3°, a movable blocking plate in front of and to one side of the detector was employed to reduce the small angle limit to -0.1°. This blocking plate served to reduce the rate of $^{12}C^{+5}$ particles entering the detector. The choices for the horizontal angular ranges were constrained by the (fixed) locations of the internal Faraday cups of the dipoles, which collected the beam particles. During the off-line analysis, the angular range was subdivided into bins corresponding to horizontal angular acceptances of

typically ±0.08°. The vertical acceptance was ±0.25° for all measurements. For purposes of display, all angles are shown as positive in our plots of angular distributions--except in the case of the ^{12}C target, where both positive and negative angles are shown.

The angle calibration was obtained by comparing the observed shift in the position of the peak from the H(^{12}C,^{12}N)n reaction with the expected kinematic shift as a function of angle. [Hydrogen was present as a contaminant in all targets; data were also taken with a $(CH_2)_n$ (polypropylene) target.] The determination of 0° was made in four ways: from the maximum in the angular distributions for the (^{12}C,^{12}N) reaction on ^{12}C, on Hydrogen in the C target, and on Hydrogen in the $(CH_2)_n$ target, and from the maximum energy for the reaction on Hydrogen (highest x-position). All of these methods agreed to within 0.1°. This angle calibration was then checked by measuring ^{12}C elastic scattering angular distributions for ^{26}Mg, ^{54}Fe and ^{90}Zr over a limited angular range (2.0° to 4.6° in the laboratory) and comparing them (in both magnitude and shape) with optical model predictions. The agreement in shape was within 0.1° for the two heavier targets. (The predictions for the ^{26}Mg target proved to be rather sensitive to the choice of optical model potentials, and no decisive result could be obtained.) The overall angular accuracy is estimated to be better than ±0.05°.

The absolute normalization of the cross sections was obtained from the target thickness and the integrated beam current measured in the Faraday cups located in the spectrograph dipoles. Different Faraday cups were needed for the ^{12}N and ^{12}B measurements, and their collection efficiencies were determined relative to a reference cup in the scattering chamber by switching from one cup to the other and back, assuming that the beam current stayed constant. The measured currents agreed to about 10%; a correction was applied to take account of this small difference. By comparing our elastic scattering cross section data with optical model calculations, we estimate the overall normalization uncertainty, arising mainly from the beam integration and the target thickness measurement, to be about ±12%.

A consistency check of the data was provided by the requirement that the cross sections measured for the two mirror reactions,

$^{12}C(^{12}C,^{12}N)^{12}B(g.s.)$ and $^{12}C(^{12}C,^{12}B)^{12}N(g.s.)$, should be identical. The measured shapes of these angular distributions were found to be similar within statistical uncertainties and their magnitudes agreed to about 10%, with that for $(^{12}C,^{12}B)$ being larger (see Fig. 9).

III. RESULTS

A. Yields for the $(^{12}C,^{12}B)$ and $(^{12}C,^{12}N)$ Reactions

Figure 1 compares spectra from the $(^{12}C,^{12}N)$ and $(^{12}C,^{12}B)$ reactions on ^{12}C. Several differences are apparent. The energy resolution (full width at half maximum) is about 280 keV ($\Delta E/E = 3.3\times10^{-4}$) for the first reaction, and about 550 keV for the second. The difference occurs because the resolution is determined by the signal to noise ratio in the drift chambers; the energy loss for boron is about one half that for nitrogen $[(5/7)^2\approx0.5]$. The other differences in the spectra reflect the different level spacings in the two final nuclei and the additional population of excited bound states in the ejectile ^{12}B. (This last possibility is absent when the ejectile is ^{12}N, since only the ground state of ^{12}N is particle-stable.)

Because ^{12}B has excited bound states, the possibility exists that the measured spectra for the $(^{12}C,^{12}B)$ reaction on all targets will exhibit peaks due to ejectile excitation. Fortunately, for all the 1^+ states of interest except one, we could rule out this possibility on the basis of the energetics of the low-lying levels of the ejectile and the final nucleus. The exception was the 1.05 MeV state in ^{58}Cu, for which (as described later) we performed a reaction calculation and concluded that the ejectile excitation contribution was negligible.

The spectra for each target were analyzed by making multiple Gaussian peak fits, keeping the widths equal and the relative positions of the peaks constant for all angles. The widths used for different targets were approximately the same for the $(^{12}C,^{12}B)$ reaction, and likewise for the $(^{12}C,^{12}N)$ reaction. A constant background was assumed; this was mainly determined by extending the region of the fit to well above the predicted ground state channel.

Spectra for $^{26}Mg(^{12}C,^{12}B)^{26}Al$ are shown in Fig. 2. The identifiable peaks correspond to excitation of the 1^+ states at 1.06, 1.85, and 2.07 MeV, the 2^+ state at 1.76 MeV and the 3^+ state at 0.42 MeV. The 1.76, 1.85, and 2.07 MeV states are not resolved and were treated as a single peak. If we assume that the yields for the 1.06, 1.85, and 2.07 MeV states scale according to their B(GT) values, which are known, about half of the observed yield for the unresolved peak around 2 MeV excitation is accounted for by the population of the two 1^+ states at 1.85 and 2.07 MeV. Note that the 5^+ ground state, indicated by the broken arrow in the lower spectrum, is very weakly excited at forward angles. Note also that there is no evidence for the excitation of the isobaric analog state at 0.24 MeV, which is as expected (except for possible small contributions from the non-local part of the exchange or spin-orbit interaction) if the reaction mechanism were one-step in nature. Inclusion of an additional peak to describe unidentified strength near 2.8 MeV, as shown in Fig. 2, made no difference to the extracted strength for the 1.06-MeV state.

Spectra for $^{54}Fe(^{12}C,^{12}B)^{54}Co$ are shown in Fig. 3. Despite the small number of counts, it was possible to make a reliable area determination for the 1^+, 0.94-MeV state of interest. Peaks at approximately 1.69 MeV and 2.44 MeV were also assumed in the fit. These may correspond to the 1.61-MeV (J=1,2) and 2.28-MeV (3^+) and/or 2.645-MeV (4^+) states in ^{54}Co seen in (^3He,t) and (p,n) studies.[16] Inclusion of these states made no significant difference in the extracted yield for the 0.94-MeV state. The rise in the yield seen at the left of the spectra corresponds to the beginning of the giant Gamow-Teller resonance, which has components at about 6.4 MeV and higher excitation.[17]

The $^{58}Ni(^{12}C,^{12}B)^{58}Cu$ spectra shown in Fig. 4 were analyzed assuming four peaks corresponding to the 1^+ ground state, the 3^+ state at 0.44 MeV, the 1^+ state of interest at 1.05 MeV, and an unresolved group of states between 1.43 and 1.65 MeV. In addition to the direct excitation of the 1.05 MeV state of ^{58}Cu, there are two other possible processes contributing to the peak seen at E_x = 1.05 MeV: (a) the excitation of ^{12}B to its 2^+, 0.95 MeV level and of ^{58}Cu to its 0^+, 0.20 MeV level; (b) the excitation of ^{12}B to its 2^+ state, with ^{58}Cu left in its 1^+ ground state. We performed one-step reaction calculations for the two processes, in a manner similar to

that described in Sect. IV, and concluded that the cross sections for (a) and (b) were only about 0.2% and 0.6%, respectively, of that of the measured peak. Thus we believe that ejectile excitation effects can be ignored for the transition of interest. The ^{58}Cu spectrum at 0.19° shows one puzzling feature, viz. the 1^+ ground-state peak is as strongly excited as the 1.05-MeV state. The B(GT) values determined for these two states from the ^{58}Ni(p,n)^{58}Cu reaction[17] are in the ratio of 1:3, so one would have expected the two states to be populated in roughly that proportion. It is possible that the "ground state" peak has some contribution from the unresolved isobaric analog state at 0.20 MeV, which might be excited by two-step (successive transfer) processes if these were not completely suppressed, or by the non-local part of the exchange or spin-orbit interaction in a one-step process. The strong peak observed at about 3.6 MeV excitation presumably corresponds to the peak seen at similar excitation in the ^{58}Ni(p,n)^{58}Cu reaction,[17] and seems to represent the excitation of several states.

It was necessary to use ±0.16° angular bins for the ^{90}Zr(^{12}C,^{12}B)^{90}Nb data to reduce the statistical fluctuations. Spectra are shown in Fig. 5. The peak at 2.3 MeV excitation is taken to correspond to that seen in the (p,n) reaction at 120 MeV,[18] where it was identified as a cluster of 1^+ states. The peak at 1.0 MeV was also observed in the (p,n) study and found to have contributions mainly from $L > 0$. The spectra were analyzed by 5-peak fits; in addition to the two peaks mentioned above, peaks at 0.0 MeV, 2.73 MeV and approximately 3.4 MeV were included in order to improve the overall quality of the fit.

Figure 6 shows spectra for the ^{56}Fe(^{12}C,^{12}N)^{56}Mn reaction. In the forward angle spectra, besides the H(^{12}C,^{12}N)n contaminant peak, two sharp and cleanly-resolved peaks are observed. From the focal plane calibration, we estimate the excitation energies in Mn for these peaks to be 0.025±0.15 MeV and 1.20±0.26 MeV. By comparison with the (t,^{3}He) spectrum of Azjenberg-Selove et al.,[19] and assuming that the spins of the states we observe are 1^+, we identify these states with the 0.11 MeV and 1.17 MeV levels in ^{56}Mn. The Hydrogen contaminant in the target interferes with the low-lying Mn states for scattering angles from about 0.3° to 1.3°. Scaling the Hydrogen peak in the 0.05° spectrum from the $(CH_2)_n$ target to the

corresponding peak in the ^{56}Fe spectrum permitted an accurate subtraction of the Hydrogen peak in the ^{56}Fe spectra. This was a significant correction only for laboratory angles of 0.53° and 1.01°. The spectra were then binned over a ±0.24° range and analyzed by making multiple Gaussian peak fits.

B. Elastic scattering angular distributions

The elastic scattering angular distributions for targets of ^{26}Mg, ^{54}Fe and ^{90}Zr measured in the present experiment are shown in Fig. 7. These data were obtained to provide tests of the optical potentials used in the charge-exchange reaction calculations, since no potentials are available in the literature for E/A = 70 MeV ^{12}C scattering. The E/A = 84 MeV $^{12}C+^{12}C$ potential from Buenerd et al.[20] yielded an angular distribution badly out-of-phase with our $^{12}C+^{26}Mg$ elastic scattering data and is not shown in Fig. 7. The three solid curves are the predictions of the E/A = 94 MeV $^{16}O+^{90}Zr$, $^{16}O+^{40}Ca$ and $^{16}O+^{28}Si$ potentials of Roussel-Chomaz et al.[21] applied to our targets of ^{90}Zr, ^{54}Fe and ^{26}Mg, respectively. The calculations give a reasonable description of the data for ^{90}Zr and ^{54}Fe. For ^{26}Mg, the calculation overpredicts the data beyond 4°. The parameters of these optical potentials are listed in Table I.

Even though the angular range of our elastic scattering data is small, Fig. 7 shows that it is adequate to distinguish among potentials determined for apparently similar projectiles, targets, and energies. For this reason we have used the present data to determine optical model parameters. The two dashed curves in Fig. 7 are the predictions of such fitted optical potentials obtained for ^{54}Fe and ^{26}Mg. These potentials (FE2 and MG2 in Table I) were constructed by first interpolating from the energy and mass trends of the volume integrals of Woods-Saxon potentials obtained by Brandan[22] and Nadasen et al.[23] and then adjusting the radii and diffusenesses to fit the elastic scattering data.

For the cases of $^{12}C+^{26}Mg$ and $^{12}C+^{54}Fe$, another approach was also used: a microscopic double-folding procedure,[24] in which the nucleon-nucleon interaction was folded with the target and projectile densities, to yield the real part of the potential. This was then supplemented by a phenomenological Woods-Saxon imaginary potential. The cross section

obtained for $^{12}C+^{26}Mg$ with this potential (not shown in Fig. 7) lies midway between the fits obtained with the two potentials whose predictions are shown in the figure. The cross section for $^{12}C+^{54}Fe$ obtained with the double-folded potential is similar to that with FE2.

C. Shapes of (^{12}C,^{12}B) and (^{12}C,^{12}N) angular distributions

One expects that the shapes of the various GT angular distributions, when plotted vs $q_\perp R$, where $q_\perp$ is the transverse component of the momentum transfer and R is the sum of the target and projectile radii, should be the same if the same reaction mechanism is dominant and if distortion effects are similar for different transitions. The magnitude of $q_\perp$ is defined in terms of the total momentum transfer q by the relation

$$q_\perp^2 = q^2 - q^2(\theta=0).$$

Diffractive effects from distortion are expected to occur at roughly the same value of $q_\perp R$, where R is the strong absorption radius. Effects due to nodes in the projectile or target transition densities at particular values of q would cause differences in shape (when plotted versus $q_\perp R$) for different reactions. In Fig. 8, the distributions for various targets are normalized by eye to that for ^{26}Mg (thick line). The expectation of similarity of shape holds roughly true, and is particularly accurate for the transition to ^{12}B(0.0 MeV), for which good-statistics data were obtained.

The angular distributions for the $^{12}C(^{12}C,^{12}N)^{12}B$(g.s.) and $^{12}C(^{12}C,^{12}B)^{12}N$(g.s.) reactions are shown in Fig. 9, for the (^{12}C,^{12}B) calibration transitions to ^{26}Al, ^{54}Co, ^{58}Cu, and ^{90}Nb in Figs. 10-11, and for the low-lying probable $0^+ \rightarrow 1^+$ transitions in the $^{56}Fe(^{12}C,^{12}N)^{56}Mn$ in Sect. VI. The curves shown in these figures are the results of the reaction calculations described in Sect. IV.

IV. DWA PREDICTIONS

Microscopic one-step Distorted Wave Approximation (DWA) calculations were performed using the code FOLD,[25] which is based upon the momentum space techniques developed by Petrovich and co-workers.[26] This formalism includes the important central ($V_{\sigma\tau}$) term in the effective interaction, including both direct and exchange in the knock-on approximation,[27] and the direct

tensor term. Effects of the spin-orbit interaction and tensor exchange, which are neglected, are expected to be small.[28,29] It is important to note the differences between this formalism and the more familiar case that arises for the (p,n) charge-exchange reaction. Because the heavy-ion projectile has internal structure, orbital angular momentum as well as spin angular momentum can be transferred in the reaction; this makes it necessary to introduce additional labels on the angular momenta involved.

The total angular momentum transferred to the projectile (target) is J_p (J_t). In the reaction studied here, $J_p = 1$; the excitation involves a transfer of spin, $S_p = 1$, and orbital angular momentum, $L_p = 0$ or 2. Notice that the heavy-ion charge-exchange reaction is necessarily more selective than the (p,n) reaction because the unnatural-parity projectile excitation will not allow excitation of Fermi transitions in the target. The target states of interest also have $J_t = 1$; they have $S_t = 1$ and $L_t = 0$ or 2. There is also a total angular momentum transfer in the relative coordinate, J_r. In the case of only central and tensor forces, as we consider here, $J_r = L_r$. Being cognizant of the fact that most readers are more familiar with the LSJ transfer language (where $L = J_r$, $S = J_p$, and $J = J_t$ for the heavy-ion case), we will use the notation L for $L_r = J_r$ in the remainder of this paper. It is important that, in the case of heavy-ion reactions, $L = 0$ in the relative coordinate does <u>not</u> select only $L_p = L_t = 0$. We will look at this issue in more detail in section IV.F.

The main ingredients in these DWA calculations are the effective interaction, the optical potentials in the entrance and exit channels, and the transition densities in the projectile and target systems. We now discuss our choices for these.

The results presented are calculated with the 100 MeV t-matrix interaction of Franey and Love[30] except for one calculation shown in Fig. 10. (This interaction was considered better for our purpose than the Franey-Love 50 MeV interaction because the former was derived by fitting to a larger range of momentum transfers in nucleon-nucleon scattering. No simple interpolation between these two interactions to 70 MeV is possible.[31]) Sample calculations were also done with the modified M3Y interaction of Petrovich et al.[32] The total cross sections predicted with

the latter were about 40% lower than those with the Franey-Love (F-L) interaction, with the L = 2 contribution relative to the L = 0 contribution being about a factor of two lower. This probably means that the tensor force, which is the dominant contributor to the L = 2 cross section, is stronger in the F-L interaction. When the results from the two interactions are separately normalized to the data, the F-L interaction gives somewhat better fits; compare the solid (F-L) and dot-dashed (M3Y) curves in Fig. 10.

The optical-model potentials obtained for ^{16}O scattering at 94 MeV/nucleon by Roussel-Chomaz et al.[21] were used for all targets except ^{12}C, for which the potential set F of Buenerd et al.[20] was used; these potentials are listed in Table I. The potentials obtained by fitting to our elastic scattering data (also given in Table I) were also tried in a few cases. While it is difficult to evaluate the uncertainties introduced by lack of optimum optical model potentials, our conclusion is that differences of perhaps 30% are possible. It was found that, for a given reaction, different optical potentials gave the same L = 0 and L = 2 shapes at forward angles but that the ratios of the L = 0 and L = 2 parts could differ by as much as 25%.

Cohen-Kurath (POT) wave functions were used to describe the projectile and ejectile.[33] For the target and residual nuclei, the wave functions used are discussed individually below. Woods-Saxon radial functions were used, with the single-particle binding energies being set equal to experimental separation energies. The transition densities corresponding to these wave functions do not exactly reproduce the experimentally known B(GT) values[17,18,34-36] for the $0^+ \rightarrow 1^+$ transitions that were used as calibrations. A correction factor was applied to take account of this, assuming that the calculated cross sections scale with B(GT), as is described below. The results are shown in Table II.

For each reaction, the calculated angular distribution (corresponding to the B(GT) used in the calculation, denoted $B(GT)_{th}$ in Table II) was fitted to the data by a least-squares procedure and the normalization factor N' was thereby obtained. N' was then scaled (divided) by the product of the ratios $B(GT)_{exp}/B(GT)_{th}$ in the projectile and target systems, to yield the normalization factor N. We expect N to be close to unity if the DWA

calculation gives an adequate description of the reaction. Departures of N from unity are a measure of the inadequacy of the parameters used in the calculations and/or of the one-step nature of the reaction mechanism itself. We note that the values of N in Table II are within about 40% of unity. Given also the reasonably good description of the shapes of the angular distributions, we take this, in conjunction with previous results,[10-12] as an indication that the reaction mechanism for these L = 0 transitions is predominantly one-step at a bombarding energy of 70 MeV/nucleon. We attribute the departures from unity mainly to uncertainties in the effective interaction and the optical potentials and to the breakdown of the assumption (tested later) that the cross sections scale with B(GT).

A. $^{12}C(^{12}C,^{12}N)^{12}B(g.s.)$ and $^{12}C(^{12}C,^{12}B)^{12}N(g.s.)$

The two reactions $^{12}C(^{12}C,^{12}N)^{12}B$ and $^{12}C(^{12}C,^{12}B)^{12}N$ leading to the ground states of the respective final nuclei should have identical differential cross sections because they are mirror reactions which involve identical particles in the entrance channel. Experimentally, as shown in Fig. 9, the magnitudes of the cross sections for the two reactions are the same to about 10%, with the values for the ($^{12}C,^{12}B$) reaction being higher overall. Compared to the $^{12}C(^{12}C,^{12}N)^{12}B(g.s.)$ cross sections of Bohlen et al.,[11,12] our results are about 60% higher, even though both measurements were made at the same bombarding energy. The reason for this is not understood despite discussions with the authors of Refs. 11 and 12. Because of the factor-of-two better resolution obtained for ($^{12}C,^{12}N$) than for ($^{12}C,^{12}B$), it was possible to obtain a more complete angular distribution for the former reaction. The symmetry around 0° of the experimental ($^{12}C,^{12}N$) angular distribution shown in Fig. 9 is further evidence that the determination of 0° is accurate.

The DWA calculations used the Cohen-Kurath (C-K) transition densities for both the projectile and target systems. The same C-K amplitudes were used for the two systems, but the isospin symmetry was broken by the use of Woods-Saxon radial functions with experimental binding energies. These radial functions resulted in different B(GT) values for the mirror ^{12}C - $^{12}N(0.0\ MeV)$ and ^{12}C - $^{12}B(0.0\ MeV)$ transitions, as shown by the

different $B(GT)_{th}$ values in Table II. This difference has long been known[37] to be caused by the different Coulomb potentials for ^{12}N and ^{12}B.

The solid curve in Fig. 9 is the result of the calculation for the $^{12}C(^{12}C, ^{12}N)^{12}B$ reaction normalized to the data. The dashed and long-dashed curves represent the contributions from the separate L = 0 and 2 parts, respectively, and their sum, which is incoherent, is shown by the solid curve. The dot-dashed curve corresponds to including only the central (direct + exchange) amplitudes, with the same normalization as for the solid curve. This figure illustrates several characteristic features of the ^{12}C-induced charge-exchange reaction at intermediate energies. First, there is an appreciable L = 2 contribution to the cross section, even at 0°. This L = 2 strength is much larger than that seen in (p,n) reactions at small angles, presumably because of the large negative Q value associated with the $(^{12}C, ^{12}N)$ reaction and the correspondingly large value of the momentum transfer at 0°, q = 0.42 fm^{-1}. It arises dominantly from the tensor force, whose strength grows rapidly with increasing momentum transfer. Second, the L = 0 and L = 2 angular distributions have distinctive shapes. Third, the tensor interaction is essential to give a good description of the angular distribution; it enhances the L = 2 contribution, which washes out the pronounced oscillations in the angular distribution calculated with the central interaction alone.

B. $^{26}Mg(^{12}C, ^{12}B)^{26}Al$

For the $^{26}Mg \rightarrow {}^{26}Al$ (1.06 MeV) transition, the full sd-shell wave functions of Brown and Wildenthal[38] were used. But even in this case, the experimental and theoretical B(GT) values differ appreciably (see Table II). The ratio of 0.58 between the two is an example of the well-known quenching of Gamow-Teller strength in nuclei.[39]

The solid and dot-dashed curves in Fig. 10 represent the full calculations with the F-L and the M3Y interactions, respectively, the two being separately normalized to the data. The F-L calculation required only a 6% normalization adjustment once the nuclear structure input was adjusted to give the correct B(GT) value (Table II), but the M3Y calculation gave a 37% lower cross section and therefore required a correspondingly higher

normalization. Apart from this difference in magnitude, the two give similar overall fits to the shape of the angular distribution, with the F-L interaction being somewhat better. The dashed and long-dashed curves in Fig. 10 are the separate L = 0 and L = 2 contributions with the F-L interaction. Compared to the case of ^{12}C in Fig. 9, the L = 2 strength relative to L = 0 is considerably smaller at the most forward angles (< 1°), probably because the Q-value for the reaction on ^{26}Mg is less negative than for ^{12}C by about 12 MeV (corresponding to q = 0.25 fm^{-1} at 0°), and therefore the momentum transfer and the tensor contribution are smaller at small angles. Consistent with this explanation, when the Q-value for ^{26}Mg is artificially set to be equal to that for the ^{12}C target, the ratio of the 0° cross section for L = 0 relative to that for L = 2 decreases by more than a factor of two (from 4.0 to 1.85).

C. $^{54}Fe(^{12}C,^{12}B)^{54}Co$ and $^{58}Ni(^{12}C,^{12}B)^{58}Cu$

For these cases transition densities were obtained from the shell-model calculations described in Sect. VI.C. The solid and dashed curves in Fig. 11 for the transition to the 0.95-MeV state in ^{54}Co represent calculations with two of the optical potentials listed in Table I (the ^{16}O + ^{40}Ca potential of Ref. 21 and the fitted FE2 potential, respectively), with the same normalization to the data. The FE2 potential (dashed curve) gives about 20% smaller cross section, but the predicted cross section shapes are similar. This also holds for the other cases.

For the 1.05-MeV state in ^{58}Cu (Fig. 11), the solid curve is again the full calculation normalized to the data. The dot-dashed curve is obtained by adjusting independently the strengths of the L = 0 and L = 2 contributions to give an optimal fit to the data (see below); the corresponding L = 0 and L = 2 contributions are shown by the dashed and long-dashed curves, respectively. We note that the dot-dashed curve gives an improved fit compared to the solid curve as the result of a 60% increase in the L = 0 and a 31% decrease in the L = 2 components. The justification for varying the L = 0 and L = 2 strengths independently is discussed later (Sect. IV.E).

D. $^{90}Zr(^{12}C, ^{12}B)^{90}Nb$

The cluster of unresolved states in ^{90}Nb at excitations near E_x = 2.3 MeV is thought to represent essentially the 1^+ member of the $(\pi g_{9/2}\nu g_{9/2}^{-1})$ multiplet.[40] DWA calculations were done using both this probable configuration and the less likely $(\pi g_{7/2}\nu g_{9/2}^{-1})$ configuration, and the separately normalized results are shown by the solid and dashed curves, respectively, for A=90 in Fig. 11. We note that the calculated shapes differ, although neither one well describes the data near 2°. This sensitivity to the choice of configuration arises because the proportion of the calculated L = 0 and L = 2 strengths depends on the configuration, although the L = 0 and L = 2 shapes do not.

E. Multipole decomposition

We have seen above that the relative L = 0 and L = 2 contributions to the calculated cross sections depend, at the 20-30% level, on the choice of the optical potential and of the effective interaction (in particular, on the relative strength of the tensor and central terms). Additional variations can arise from differences in the specific transition densities used in the DWA calculations. On the other hand, the L = 0 and L = 2 angular distribution shapes themselves are nearly insensitive to these choices and have distinctive shapes. Given this situation, we adopted the procedure of independently adjusting the strengths of the L = 0 and L = 2 contributions to give a best fit (minimum χ^2) to the measured angular distributions. This procedure, which is equivalent to performing a multipole decomposition, generally resulted in good fits to the measured angular distributions; as an example, see the dot-dashed curve in Fig. 11 for ^{58}Ni. The resulting normalization factors N'(L=0) and N'(L=2), as well as N(L=0) which has been renormalized to the experimental B(GT) values in the same way as the N values in Table II, are listed in Table III. N'(L=2) is not similarly renormalized because the L = 2 cross section is not a model-independent measure of B(GT), as we shall see in Sect. IV.F. The closeness of the values of N'(L=0) and N'(L=2) to each other indicates the extent to which the original distorted-wave calculations agreed with the experimental angular distributions. We note from Table III that the

original calculations gave almost as good a fit as the multipole-decomposition fits for the cases of the ^{12}C, ^{26}Mg, and ^{54}Fe targets, but not for ^{58}Ni or ^{90}Zr. The percentage improvements in χ^2 produced by the multipole-decomposition fits are listed in Table III.

F. Further studies using the DWA calculations

In order to establish the utility of the (^{12}C,^{12}B) and (^{12}C,^{12}N) reactions as spin probes, we performed a number of computational tests for $0^+ \rightarrow 1^+$ transitions using DWA calculations. The first issue studied was the magnitude of the additional amplitudes that are present in the heavy-ion charge-exchange reaction compared to the nucleon case. Recall, from the discussion at the beginning of Sec. IV, that the transfer of $J_p = 1$ to the projectile in a $0^+ \rightarrow 1^+$ transition can be accomplished by either $L_p = 0$ or 2. This additional degree of freedom, transfer of orbital angular momentum to the projectile, greatly complicates the way particular target transitions are sampled for particular relative L transfers. [The details can be deduced from Eq. (22) and Table 3 in Ref. 26, and Eq. (31b) of that reference explicitly shows the terms that appear when both projectile and target undergo a $0^+ \rightarrow 1^+$ transition.] The essential point is that the non-central character of the tensor force causes "cross terms", i.e. $L_p = 0$ coupled with $L_t = 2$ and vice versa, to appear in the L = 0 cross section and "GT terms", i.e. $L_p = 0$ coupled to $L_t = 0$, to appear in the L = 2 cross section. In addition, terms with $L_p = L_t = 2$ will appear in the L = 0 cross section. These $L_p = 2$ contributions cannot occur in the nucleon charge-exchange case because the projectile is regarded as a point object.

The issue we must address is whether, despite the significant $L_p = 2$ contribution to the L = 0 cross section, the transitions are predominantly Gamow-Teller in the target system (i.e. $L_t = 0$). To this end, the effect of setting specific parts of the projectile and target densities to zero was investigated. Figure 12 shows the separate contributions from the $L_t = 0$ and $L_t = 2$ parts of the target density for the $^{26}Mg(^{12}C,^{12}B)^{26}Al$ reaction; their coherent sum is the total cross section given by the solid curve. This shows that the cross section is dominated by the Gamow-Teller part in the target system ($L_t = 0$). It was similarly found that the Gamow-Teller

part in the projectile system ($L_p = 0$) is dominant. Similar results were found for the other nuclei we studied.

Comparison of the results in Fig. 12 to those shown in Fig. 10 will serve to further illustrate the physics of this reaction. We note from Fig. 12 that contributions with $L_t = 2$ are two orders of magnitude lower (hence essentially negligible) than those with $L_t = 0$ at all angles, and yet we see a substantial $L = 2$ contribution to the cross section in Fig. 10. One would deduce, correctly, that the "cross terms" cannot be responsible; they are responsible for the relatively small difference between the dashed and dot-dashed curves in Fig. 9. Instead, the large $L = 2$ contribution arises from $L_p = 0$ transfer coupled to $L_t = 0$ transfer by the tensor interaction. Thus both the $L = 0$ and $L = 2$ parts of the cross section are driven essentially by the GT densities and tend to isolate the central and tensor interaction contributions, respectively. However, the tensor coupling brings in a q^2 dependence so that the $L = 2$ part is not a model-independent measure of B(GT). This expectation is verified by the results in Fig. 13 below.

Even though the comparisons above show that the Gamow-Teller parts of the target and projectile densities dominate the cross section, we still need to ascertain to what extent the cross sections can provide a quantitative measure of GT strength. The point here is that heavy-ion reactions sample only the surface parts of the GT transition densities. It follows that they sample the target transition density over a large range in the momentum transfer q, rather than the density near $q = 0$ which fixes B(GT). One might then expect that B(GT) can be extracted only if the transition densities for different GT states have approximately the same q dependence. On the other hand, when we examined the extent to which the $L = 0$ parts of the cross sections are proportional to B(GT) values for different transitions in the case of $^{26}Mg(^{12}C, ^{12}B)^{26}Al$, a good correlation was found. Cross sections for the first six 1^+ states in the shell-model spectrum[38] of ^{26}Al (at $E_x = 0.74$, 1.66, 1.92, 2.82, 3.60, and 4.86 MeV) were computed and their ratios to B(GT) values calculated with the same wave functions were examined. The results, shown in Fig. 13, indicate that this ratio is nearly constant even for weak GT transitions such as those to states 4 and 5. The horizontal long-dashed line is drawn at the average

value of the ratios for the 0°, L = 0 part of the cross sections; the average deviation from proportionality is only about 11%. This shows that the L = 0 cross section is essentially proportional to B(GT) even for states with widely varying B(GT) values. We note that the L = 2 part of the cross section is not proportional to the GT strength, although the sum, L=0+2, is approximately proportional because $\sigma(L=0) >> \sigma(L=2)$. The horizontal solid line is drawn at the average value of the ratios for this sum.

In Fig. 14, we show the q-dependence of the transition density for two of the states considered in Fig. 13, viz. those with the highest and the lowest B(GT) values (states 1 and 5, respectively). It is evident that the densities have different behaviors for q greater than about 1 fm^{-1}, e.g. state 1 has a node but state 2 does not. Yet, despite this difference in q-dependence and despite the factor of 66 difference in the B(GT) values, the ratio of L = 0 cross section to B(GT) is nearly the same for the two states (Fig. 13). We have undertaken a theoretical study[13] which gives some indication of why $\sigma(L=0)$ is a reasonably good measure of B(GT), even when the q dependences of the transition densities differ, as is the case here.

We also performed a calculation for a 0^+ to 1^+ transition which was guaranteed to be non-GT in character, viz. the $[f_{5/2}p_{3/2}^{-1}]_{1^+}$ transition in the $^{56}Fe(^{12}C, ^{12}N)$ reaction. This is a non-GT transition because it allows only $L_t = 2$. It was found that the L = 0 part of the cross section, which comes entirely from the tensor part of the interaction, was negligibly small. This shows again that the $L_t = 2$ part of the target transition density contributes negligibly to the L = 0 part of the cross section.

These computational studies encourage us to believe that the L = 0 part of the charge-exchange cross section may be taken as a measure of the GT strength in the target transition density. The analysis of our experimental cross sections based on a multipole decomposition of the L = 0 contribution to the cross section is presented in Sect. V.

V. CROSS SECTIONS COMPARED WITH β-DECAY MATRIX ELEMENTS

The following procedure was used to obtain the unit cross sections, the ratio of the experimental cross section extrapolated to q = 0 to the GT

strength B(GT). First, as described above, DWA calculations were done to provide L = 0 and L = 2 angular distributions. The relative strengths of these distributions were adjusted to yield an optimal fit to the cross section, corresponding to a minimum in χ^2. This yielded the L = 0 cross section at 0°, i.e. at zero transverse momentum transfer. In order to obtain the cross section corresponding to zero total momentum transfer (q = 0), this cross section was multiplied by the ratio, F(Q), of the L = 0 cross section calculated at Q = 0 to that at the actual Q of the reaction (typically around -20 to -30 MeV). Dividing this cross section by the corresponding B(GT) gives $\hat{\sigma}$, the cross section per unit GT strength. The results are shown in Table IV and plotted in Fig. 15. The dashed and the dot-dashed curves shown in Fig. 15 were obtained assuming a linear and a quadratic form, respectively, for the A-dependence of $\hat{\sigma}$. These assumptions were made in the absence of any theoretical input as to the A-dependence. The parameters of the fits, determined by least-squares fittings in which the data points were weighted by their relative uncertainties, are:

$\hat{\sigma}$ = (4.078±0.390) - (0.0382±0.006)A (linear fit);

$\hat{\sigma}$ = (6.275±0.794) - (0.134±0.030)A + [(0.814±0.256)/1000]A^2 (quadratic fit).

The sources of relative uncertainty in $\hat{\sigma}$ include the following: the statistical error in the measured cross section, varying from ±6.5% for A = 12 to ±12% for A = 90; the uncertainty in the procedure for obtaining σ(L=0,θ=0,Q=0), which was estimated to be ±10% by using different optical potentials, effective interactions, and final-nucleus configurations; and the uncertainty in B(GT), which (as given in Table II) ranges from ±0.7% for A = 12 to ±20% for A = 58 and 90. These uncertainties were added in quadrature to yield the overall uncertainties shown in Table IV. The uncertainty in the absolute cross section determination (±12%) was not included in this procedure. We note that the biggest source of uncertainty for A = 58 and 90 is that coming from B(GT).

The calibration curves thus determined are essentially phenomenological in nature and not dependent on detailed reaction calculations; for example, they are relatively insensitive to the choice of optical potentials used to extrapolate to q=0, since that procedure involves only the ratio of two calculated cross sections. These calibration curves can be used to obtain the B(GT) value from the cross section measured for an unknown transition.

Their application in the determination of β^+ GT strengths from the cross sections measured for the $^{56}Fe(^{12}C,^{12}N)^{56}Mn$ reaction is described in Sect. VI.

VI. GAMOW-TELLER STRENGTHS IN ^{56}Mn

A. Electron Capture Rates For Elements Near the Fe Peak

Electron capture affects the evolution of stars toward and through their supernova stages.[5] As the star evolves through its oxygen and silicon burning stages, the size of the central iron core formed depends on electron capture and β-decay rates in the upper-sd- and fp-shell nuclei. Later, after the iron core has evolved, the nature of the ensuing core collapse depends on the electron capture rate because of its effect on the density of free electrons. The supernova process is also affected by neutrino-induced charged current reactions, which are sensitive to the same matrix elements and are a source of heating during the supernova expansion.[41]

For the important nuclei, experimental information on the Gamow-Teller strength governing these processes is limited. The collective Gamow-Teller strength is not energetically accessible to β decay in N > Z nuclei and charge-exchange reactions used in the past either have relatively low energy resolution [(n,p)] or present reaction mechanism problems [(t,^{3}He) at low energies]. Consequently, estimates of supernova behavior have mainly relied on theoretical β^+ rates[14] which have not been tested against experiment in detail and which depend sensitively on the amount of configuration mixing in the wave functions. To address this issue experimentally in one specific case, we present the results for GT β^+ strengths in transitions to ^{56}Mn.

B. Results from the $^{56}Fe(^{12}C,^{12}N)^{56}Mn$ Reaction

As stated in Sect. III.A, the identification of the peaks at E_x = 0.11 and 1.17 MeV in the spectra shown in Fig. 6 as 1^+ states in ^{56}Mn is based on results from low-energy $^{56}Fe(^3He,t)$ work, where they are the two strongest 1^+ states seen. Inspection of Fig. 6 shows that, with the energy resolution achieved, no other states are resolved. The angular distributions for the two isolated 1^+ states are shown in Fig. 16, along with the results of DWA

calculations normalized to the data. The DWA calculations used shell-model wave functions obtained as described in Sect. VI.C. Next, a multipole decomposition of the two angular distributions was done in the manner described in Sect. V. The normalizations N'(L=0) and N'(L=2) thus obtained are listed in Table V. We use the notation N' rather than N to signify that the DWA cross sections are not scaled by the experimental B(GT) values for these states, which are unknown to begin with. Inspection of the N'(L=0) and N'(L=2) values shows that the transition to the 0.11-MeV state has more L = 2 strength than predicted with the shell-model wave functions used, whereas that for the 1.17-MeV state is correctly predicted as regards the relative L = 0 and L = 2 contributions.

From the L = 0 cross section data, $\sigma(L=0,\theta=0,Q=0)$ values for the two transitions were obtained in the same way as described in Sect. V. They are listed in the last column of Table V. To convert these values to B(GT), the unit cross section $\hat{\sigma}$ at A=56 was read off from the two calibration curves shown in Fig. 15. The values of $\hat{\sigma}(A=56)$ determined by the linear and the quadratic calibrations are 1.94 and 1.35 mb/sr, respectively. The average of these was used to convert $\sigma(L=0,\theta=0,Q=0)$ to B(GT). The uncertainty in B(GT) was determined by adding in quadrature the statistical error in the measured cross sections (±17%), the error in the procedure for extrapolating to $\theta=0$ and $Q=0$ (±10%), and the uncertainty in $\hat{\sigma}$ corresponding to half the difference between the linear and the quadratic fits (±18%). The B(GT) values thus obtained were then corrected for the fact that the reaction used to measure the A=56 cross sections was (^{12}C, ^{12}N) whereas the calibration curves of Fig. 15 are based on data from the (^{12}C, ^{12}B) reaction. Since the B(GT) values for the ^{12}C - ^{12}N and ^{12}C - ^{12}B transitions are different by 13%, as shown in Table II, the (^{12}C, ^{12}N) and (^{12}C, ^{12}B) cross sections are different because they scale (to first order) with the B(GT) in the projectile-ejectile system. The B(GT) values extracted for ^{56}Mn were therefore increased by 13%.

The B(GT) values obtained by the above procedure for the 1^+ states at E_x = 0.11 and 1.17 MeV in ^{56}Mn are shown in Table VI, where they are compared with the results of three shell-model calculations described in Sect. VI.C. The extracted strengths appear to agree better with our calculated results than with those of Bloom and Fuller.[14] The average

quenching factor for the sum of the two transitions obtained by comparing the extracted strengths to Bloom and Fuller's calculation, our calculation in the smaller model space, and our calculation in the larger model is 0.49, 0.70, and 0.75, respectively. These factors are somewhat larger than those obtained from a comparison of the results for the $^{54}Fe(n,p)^{54}Co$ reaction[3] with the calculation of Ref. 14, although the uncertainties are substantial. Calculations of the supernova process have previously been made[42] using the results of Ref. 14. It remains to be seen how these calculations will be affected by the different B(GT) values obtained in the present experiment.

C. Shell-Model Calculations

In order to interpret the experimental results for the fp-shell nuclei studied, shell-model calculations were performed for A = 54, A = 56, and A = 58. Following the procedure discussed by Wang et al.,[43] a model-space truncation was adopted which allowed at most one particle to be excited. The interaction used was that of Van Hienen et al.[44] for two-body matrix elements in the $f_{5/2}$, $p_{3/2}$, $p_{1/2}$ space and of Koops and Glaudemans[45] for the additional matrix elements introduced by the inclusion of the $f_{7/2}$ orbital. This combination was found to give a reasonable description of the level sequence and spacings of the low-lying levels of ^{54}Fe. The calculations were carried out with the shell-model code OXBASH.[46]

The A = 54 and A = 58 calculations done were for the β^- transitions from ^{54}Fe and ^{58}Ni ground states to the T = 0, 1^+ levels of ^{54}Co and ^{58}Cu, respectively. The A = 56 calculation was for the β^+ transition from ^{56}Fe ground state to the T=3, 1^+ levels of ^{56}Mn. Calculations for these transitions, using various interactions and model spaces, have been done previously, by Gaarde et al.[47] for A = 54, Bloom and Fuller[14] for A = 56, and Rapaport et al.[48] for A = 58. The main motivation for our A = 54 and A = 58 calculations was to get realistic transition densities for the DWA calculations in Sect. IV.C; this was important because DWA calculations done using simple configurations showed that the shape of the calculated angular distribution at very forward angles was sensitive to the choice of the configuration. For the A = 56 case, we were also interested in a comparison of the β^+ strengths extracted from the data with the shell-model predictions. Only the results for A = 56 are presented here.

For the A = 56 case, the zero-order model is a 2p2h configuration for the initial state and a 3p3h configuration for the final state, the transition being from

$[\pi(f_{7/2})^{-2}\nu(p_{3/2}, p_{1/2}, f_{5/2})^{2}]$ to $[\pi(f_{7/2})^{-3}\nu(p_{3/2}, p_{1/2}, f_{5/2})^{3}]$.

This is the model space used in Ref. 14. We performed calculations with this model space as well as with a larger space in which 1p1h excitations into the $f_{5/2}$, $p_{3/2}$, and $p_{1/2}$ orbitals in both the initial and final nuclei were included, resulting in 3p3h configurations in the ground state and 4p4h configurations in the final state. (Similar model spaces were used for the A = 54 and A = 58 calculations.)

It was found that the calculated GT^+ strength is mainly concentrated in the first few MeV of excitation in ^{56}Mn and that almost the entire strength is exhausted in the first 8 MeV of excitation. These features are shown in Fig. 17. The total GT^+ strength calculated with the larger model space is $S_{\beta^+} = 7.38$, which is 20% lower than the strength of $S_{\beta^+} = 9.25$ found with the zero-order model space. Bloom and Fuller obtained $S_{\beta^+} = 10.00$ with their zero-order calculation. The comparison of strengths between experiment and theory for individual states in ^{56}Mn is shown in Table VI and was discussed in Sect. VI.B. Table VI shows that there is a significant dependence on the two-body interaction, more than on the model space, for the strengths of individual states if not for the sum strength. There is no clear evidence in our experimental spectra (Fig. 6) for the major strength predicted near $E_x = 2.5$ MeV.

VII. CONCLUSIONS

The utility of heavy-ion charge-exchange reactions for spin physics studies has been examined and the results are encouraging. A comparison of the cross sections measured for the (^{12}C, ^{12}B) reaction at E/A = 70 MeV on a variety of targets with the results of DWA calculations shows that $0^+ \rightarrow 1^+$ transitions are predominantly one-step at that bombarding energy. The calculated cross sections are generally in good agreement with the measured cross sections, requiring renormalizations that are typically less than 40%, which is in the range of the overall calculational and experimental uncertainties. In many cases the angular distributions are well described quantitatively.

A correlation between cross sections and the Gamow-Teller strengths B(GT) for the corresponding transitions has been found both empirically and computationally. Empirically, the correlation was established using the (^{12}C,^{12}B) reaction to excite states with known B(GT); a weak dependence on the target mass was observed for A > 12. Computationally, the correlation was studied by examining the proportionality between cross sections calculated for six $0^+ \rightarrow 1^+$ transitions to ^{26}Al and the B(GT) values calculated with the same wave functions; the average deviation from proportionality was found to be about 11%, even though the B(GT) values ranged over two orders of magnitude.

The existence of such correlations is perhaps surprising in view of the strong absorption in heavy-ion reactions. The strong absorption implies that the reaction is localized in space and therefore samples a wide range of the momentum transfer in the projectile and target transition densities. This should make the reaction a poor measure of Gamow-Teller strength, which is determined by the transition density at zero momentum transfer. Why strong correlations are found empirically and computationally deserves further study.[13] It is significant that similar strong correlations have been found experimentally for another heavy-ion charge-exchange reaction, the (^{6}Li,^{6}He) reaction.[7]

We have used the empirical calibration curve to determine B(GT) values for two low-lying 1^+ levels in ^{56}Mn from the cross sections measured for the ^{56}Fe(^{12}C,^{12}B)^{56}Mn reaction. The results are compared with shell-model calculations performed by Bloom and Fuller[14] earlier and by us for the present study, and are found to be in better agreement with the latter. The calculated B(GT) values have a significant dependence on both the two-body interaction and the model spaces involved. Further measurements such as those presented here will be required to constrain the shell-model calculations so as to facilitate reliable calculations for transitions which are important in astrophysical phenomena but which cannot be measured in the laboratory. This is particularly important because it appears that individual transitions can sometimes have an important effect in presupernova stars.[49]

Finally, it seems clear that higher energies will be necessary to reduce the uncertainties presently involved in heavy-ion charge-exchange reactions and to take advantage of their full potential. There are two principal reasons for this conclusion. The first is that, for a given transition, the momentum transfer at 0° decreases as the bombarding energy increases, increasing the ratio of L = 0 to L = 2 strength. For example, in the case of $^{26}Mg(^{12}C,^{12}B)^{26}Al(1^+, 1.06\ MeV)$, the ratio of L = 0 to L = 2 is 4 at E/A = 70 MeV and 5.4 at E/A = 150 MeV, all else being constant. The second reason concerns the importance of successive transfer reactions which may obscure the direct charge-exchange reactions in which we are most interested. Lenske et al.[12] have shown that for transitions with L > 0, successive transfer processes may be important for the ($^{12}C,^{12}N$) reaction unless bombarding energies are well above E/A = 100 MeV.

ACKNOWLEDGMENTS

We are grateful to M.B. Aufderheide, G.F. Bertsch, B.A. Brown, and F. Osterfeld for several useful conversations. We thank E. Adamides and A. Nadasen for providing assistance with data analysis and with elastic scattering optical model fits, respectively. We acknowledge correspondence with H.G. Bohlen, M. Buenerd, H. Lenske and W. von Oertzen regarding the comparison between their measurements and ours on the ^{12}C target. S.D. Bloom provided clarification on the shell-model calculations of Ref. 14. Those of us who were visitors at GANIL express thanks for the hospitality and technical assistance of the GANIL staff. One of the authors (J.A.C) acknowledges the warm hospitality of the National Superconducting Cyclotron Laboratory during his visit in 1989. This research was supported in part by the U.S. National Science Foundation under Grants PHY86-11210 and PHY89-13815 and by the U.S. Department of Energy under Contract Number DE-FC05-85ER250000.

REFERENCES

[a]Present address: Department of Physics, University of South Carolina, Columbia, South Carolina 29208.

[b]Present address: DPhN, Centre d'Etudes Nuclèaires de Saclay, 91191 Gif sur Yvette, France.

[c]Present address: Institute of Modern Physics, Lanzhou, China.

[1] C.D. Goodman, C.A. Goulding, M.B. Greenfield, J. Rapaport, D.E. Bainum, C.C. Foster, W.G. Love, and F. Petrovich, Phys. Rev. Lett. **44**, 1755 (1980).

[2] T.N. Taddeucci, C.A. Goulding, T.A. Carey, R.C. Byrd, C.D. Goodman, C. Gaarde, J. Larsen, D. Horen, J. Rapaport, and E. Sugarbaker, Nucl. Phys. **A469**, 125 (1987).

[3] M.C. Vetterli, O. Häusser, R. Abegg, W.P. Alford, A. Celler, D. Frekers, R. Helmer, R. Henderson, K.H. Hicks, K.P. Jackson, R.G. Jeppeson, C.A. Miller, K. Raywood, and S. Yen, Phys. Rev. C **40**, 559 (1989).

[4] K.P. Jackson, A. Celler, W.P. Alford, K. Raywood, R. Abegg, R.E. Azuma, C.K. Campbell, S. El-Kateb, D. Frekers, P.W. Green, O. Häusser, R.L. Helmer, R.S. Henderson, K.H. Hicks, R. Jeppeson, P. Lewis, C.A. Miller, A. Moalem, M.A. Moinester, R.B. Schubank, G.G. Shute, B.M. Spicer, M.C. Vetterli, A.I. Yavin, and S. Yen, Phys. Lett. **201B**, 25 (1988).

[5] H. Bethe, G.E. Brown, J. Applegate, and J.M. Lattimer, Nucl. Phys. **A324**, 487 (1979).

[6] O. Häusser, Invited talk at 23rd Yamada Conference on Nuclear Weak Process and Nuclear Structure, Osaka, June 1989.

[7] N. Anantaraman, J.S. Winfield, S.M. Austin, Z. Chen, A. Galonsky, J. van der Plicht, C.C. Chang, G. Ciangaru, and S. Gales, Phys. Rev. Lett. **57**, 2375 (1986); J.S. Winfield, N. Anantaraman, S.M. Austin, Z. Chen, A. Galonsky, J. van der Plicht, H.-L. Wu, C.C. Chang, and G. Ciangaru, Phys. Rev. C **35**, 1734 (1987).

[8] H. Wirth, E. Aschenauer, W. Eyrich, A. Lehmann, M. Moosburger, H. Schlösser, H.J. Gils, H. Rebel, and S. Zagromski, Phys. Rev. C **41**, 2698 (1990).

[9] M. Moosburger, E. Aschenauer, H. Dennert, W. Eyrich, A. Lehmann, R. Rudeloff, H. Schlösser, H. Wirth, H.J. Gils, H. Rebel, and S. Zagromski, Phys. Rev. C **41**, 2925 (1990).

[10] J.S. Winfield, N. Anantaraman, S.M. Austin, L.H. Harwood, J. van der Plicht, H.-L. Wu, and A.F. Zeller, Phys. Rev. C **33**, 1333 (1986); C **35**, 1166 (1987) [E].

[11] H.G. Bohlen, B. Gebauer, D. Kolbert, S. Kubono, W. von Oertzen, P.O. Pellegrin, E. Stiliaris, M. Wilpert, T. Wilpert, H. Lenske, H.H. Wolter, A. Miczaika, N. Alamanos, J. Barrette, B. Berthier, B. Fernandez, J. Gastebois, C. Berat, M. Buenerd, J.Y. Hostachy, Ph. Martin, and W. Mittig, Nucl. Phys. **A488**, 89c (1988).

[12] H. Lenske, H.H. Wolter, and H.G. Bohlen, Phys. Rev. Lett. **62**, 1457 (1989).

[13] F. Osterfeld, N. Anantaraman, S.M. Austin, G.F. Bertsch, J.A. Carr, and J.S. Winfield, to be published.

[14] S.D. Bloom and G.M. Fuller, Nucl. Phys. **A440**, 511 (1985).

[15] L. Bianchi, B. Fernandez, J. Gastebois, A. Gillibert, W. Mittig, and J. Barrette, Nucl. Instrum. Methods **A276**, 509 (1989).

[16] Wang Gongqing, Zhu Jiabi, and Zhang Jingen, Nucl. Data Sheets **50**, 255 (1987).

[17] J. Rapaport, T. Taddeucci, T.P. Welch, C. Gaarde, J. Larsen, D.J. Horen, E. Sugarbaker, P. Koncz, C.C. Foster, C.D. Goodman, C.A. Goulding, and T. Masterson, Nucl. Phys. **A410**, 371 (1983).

[18] D.E. Bainum, J. Rapaport, C.D. Goodman, D.J. Horen, C.C. Foster, M.B. Greenfield, and C.A. Goulding, Phys. Rev. Lett. **44**, 1751 (1980).

[19] F. Ajzenberg-Selove, R.E. Brown, E.R. Flynn, and J.W. Sunier, Phys. Rev. C **30**, 1850 (1984); C **31**, 777 (1985).

[20] M. Buenerd, A. Lounis, J. Chauvin, D. Lebrun, P. Martin, G. Duhamel, J.C. Gondrand, and P. de Saintignon, Nucl. Phys. **A424**, 313 (1984).

[21] P. Roussel-Chomaz, N. Alamanos, F. Auger, J. Barrette, B. Berthier, B. Fernandez, and L. Papineau, Nucl. Phys. **A477**, 345 (1988).

[22] M.E. Brandan, Phys. Rev. Lett. **60**, 784 (1988).

[23] A. Nadasen, M. McMaster, M. Fingal, J. Tavormina, P. Schwandt, J.S. Winfield, M.F. Mohar, F.D. Becchetti, J.W. Jänecke, and R.E. Warner, Phys. Rev. C **39**, 536 (1989).

[24] G.R. Satchler and W.G. Love, Phys. Rep. **55**, 183 (1979).

[25] J. Cook and J.A. Carr, computer program FOLD, Florida State University 1988 (unpublished); this is based on the code originally used in F. Petrovich and D. Stanley, Nucl. Phys. **A275**, 487 (1977), modified as described in J. Cook, K.W. Kemper, P.V. Drumm, L.K. Fifield, M.A.C. Hotchkis, T.R. Ophel, and C.L. Woods, Phys. Rev. C **30**, 1538 (1984) with additions to handle the Woods-Saxon radial functions and other specifics important for the present calculations.

[26] F. Petrovich, R.J. Philpott, A.W. Carpenter, and J.A. Carr, Nucl. Phys. **A425**, 609 (1984), and references therein.

[27] M. Golin, F. Petrovich, and D. Robson, Phys. Lett. **64B**, 253 (1976).

[28] T. Udagawa, A. Schulte, and F. Osterfeld, Nucl. Phys. **A474**, 131 (1987).

[29] A. Etchegoyen, E.D. Izquierdo, and M.C. Etchegoyen, Phys. Lett. **231B**, 224 (1989).

[30] M.A. Franey and W.G. Love, Phys. Rev. C **31**, 488 (1985).

[31] W.G. Love, private communication.

[32] F. Petrovich, R.H. Howell, C.H. Poppe, S.M. Austin, and G.M. Crawley, Nucl. Phys. **A383**, 355 (1982).

[33] S. Cohen and D. Kurath, Nucl. Phys. **73**, 1 (1965).

[34] F. Ajzenberg-Selove, Nucl. Phys. **A433**, 1 (1985).

[35] R. Madey, B.S. Flanders, B.D. Anderson, A.R. Baldwin, C. Lebo, J.W. Watson, S.M. Austin, A. Galonsky, B.H. Wildenthal, and C.C. Foster, Phys. Rev. C **35**, 2011 (1987).

[36] B.D. Anderson, private communication.

[37] I.S. Towner, Nucl. Phys. **A216**, 589 (1973).

[38] B.H. Wildenthal, Prog. Part. Nucl. Phys. **11**, 5 (1984); B.A. Brown and B.H. Wildenthal, Ann. Rev. Nucl. Part. Sci. **38**, 29 (1988).

[39] B.A. Brown and B.H. Wildenthal, At. Data Nucl. Data Tables **33**, 347 (1985).

[40] R.R. Doering, A. Galonsky, D.M. Patterson, and G.F. Bertsch, Phys. Rev. Lett. **35**, 1691 (1975).

[41] W.C. Haxton, Phys. Rev. Lett. **60**, 1999 (1988).

[42] G.M. Fuller, W.A. Fowler, and M.J. Newman, Ap. J. **293**, 1 (1985).

[43] D. Wang, J. Rapaport, D.J. Horen, B.A. Brown, C. Gaarde, C.D. Goodman, E. Sugarbaker, and T.N. Taddeucci, Nucl. Phys. **A480**, 285 (1988).

[44] J.F.A. Van Hienen, W. Chung, and B.H. Wildenthal, Nucl. Phys. **A269**, 159 (1976).

[45] J.E. Koops and P.W.M. Glaudemans, Z. Phys. **A 280**, 181 (1977).

[46] A. Etchegoyen, W.D.M. Rae, and B.A. Brown, MSU-NSCL report no. 524 (1984), unpublished.

[47] C. Gaarde, J.S. Larsen, A.G. Drentje, M.N. Harakeh, S.Y. van der Werf, and A. Müller-Arnke, Nucl. Phys. **A346**, 497 (1980).

[48] J. Rapaport, T. Taddeucci, T.P. Welch, D.J. Horen, J.B. McGrory, C. Gaarde, J. Larsen, E. Sugarbaker, P. Koncz, C.C. Foster, C.D. Goodman, C.A. Goulding, and T. Masterson, Phys. Lett. **119B**, 61 (1982).

[49] M.B. Aufderheide, G.E. Brown, T.T.S. Kuo, D.B. Stout, and P. Vogel, Ap. J. **362**, 241 (1990).

Table I. Woods-Saxon optical model potentials. "System" and "E/A" refer to the scattering system and bombarding energy for which the potential was derived. The convention $R = r(A_T^{1/3}+A_P^{1/3})$ is used. Potential strengths are in MeV, radii and diffusenesses are in fm, and volume integrals are in MeV.fm^3.

System	E/A	V	r_v	a_v	W	r_w	a_w	J_v/A	J_w/A	Ref.
$^{12}C+^{12}C$	84	120	0.71	0.84	34.0	0.96	0.69	125	69	20
$^{16}O+^{28}Si$	94	100	0.892	0.905	50.5	0.992	0.780	151	95	21
$^{16}O+^{40}Ca$	94	60	1.042	0.710	54.1	1.042	0.710	105	95	21
$^{16}O+^{90}Zr$	94	129	0.946	0.790	124.1	0.946	0.790	124.	120.	21
$^{12}C+^{26}Mg$	70	82	0.863	0.901	38.0	0.917	1.110	143	87	(a)
$^{12}C+^{26}Mg$	70	-	-	-	38.0	0.921	1.265	236	97	(b)
$^{12}C+^{54}Fe$	70	96	0.971	0.748	59.0	0.929	1.027	146	91	(a)
$^{12}C+^{54}Fe$	70	-	-	-	59.3	0.919	1.092	228	92	(b)

a) Fitted Woods-Saxon potential (denoted in the text as MG2 and FE2 for ^{26}Mg and ^{54}Fe targets, respectively).

b) Woods-Saxon imaginary potential used in conjunction with real folded potential.

Table II. Experimental and theoretical B(GT) values for the Gamow-Teller transitions shown. Their ratio is used to renormalize the ratio N' of the measured to the calculated cross section for (^{12}C, ^{12}B) reactions at E/A = 70 MeV. The renormalized ratio is denoted N. The references are to the sources of the $B(GT)_{exp}$ values.

Transition	$B(GT)_{exp}$	$B(GT)_{th}$	N'	N	Ref.
^{12}C - ^{12}N(0.0 MeV)	0.882±0.006	0.755	0.95	0.67	34
^{12}C - ^{12}B(0.0 MeV)	0.996±0.007	0.824	(a)	(a)	34
^{26}Mg - ^{26}Al(1.06 MeV)	1.09±0.05	1.90	0.65	0.94	35
^{54}Fe - ^{54}Co(0.94 MeV)	0.74±0.07	1.14	0.44	0.57	36
^{58}Ni - ^{58}Cu(1.05 MeV)	0.50±0.10	0.27	1.45	0.64	17
^{90}Zr - ^{90}Nb(2.31 MeV)	1.8±0.36	12.21	0.25	1.39	18

a) Cross section not fitted to DWA calculation.

Table III. Normalizations obtained by independently adjusting the strengths of the L = 0 and L = 2 contributions to give the best fits to the (^{12}C, ^{12}B) angular distributions for the transitions shown. N is obtained from N' by renormalizing to the experimental B(GT) values. $\Delta\chi^2$ is the percentage improvement in χ^2 resulting from the independent adjustment.

Transition	N'(L=0)	N'(L=2)	N(L=0)	$\Delta\chi^2$ (%)
^{12}C - ^{12}B(0.0 MeV)	1.06	0.92	0.75	1.7
^{26}Mg - ^{26}Al(1.06 MeV)	0.57	0.74	0.82	9.5
^{54}Fe - ^{54}Co(0.94 MeV)	0.38	0.48	0.49	7.6
^{58}Ni - ^{58}Cu(1.05 MeV)	2.32	0.98	1.03	48.2
^{90}Zr - ^{90}Nb(2.31 MeV)	0.18	0.39	1.00	15.4

Table IV. The cross section per unit B(GT), $\hat{\sigma}$, as a function of target mass, determined from (^{12}C,^{12}B) data at E/A = 70 MeV using the procedure described in the text. F(Q) is the ratio of the L=0 cross section at Q=0 to that calculated at the actual Q of the reaction. $\sigma(L=0,\theta=0,Q=0)$ is obtained by multiplying the estimated experimental cross section at $\theta=0$, $\sigma(L=0,\theta=0)$, by F(Q).

Target	$\sigma(L=0,\theta=0)$ mb/sr	F(Q)	$\sigma(L=0,\theta=0,Q=0)$ mb/sr	$\hat{\sigma}$ mb/sr
^{12}C	0.702	6.81	4.78	5.42±0.65
^{26}Mg	1.762	1.84	3.24	2.98±0.39
^{54}Fe	0.408	2.38	0.97	1.31±0.27
^{58}Ni	0.559	2.46	1.38	2.75±0.67
^{90}Zr	0.839	1.77	1.48	0.82±0.21

Table V. Results from the $^{56}Fe(^{12}C, ^{12}N)^{56}Mn$ reaction for two 1^+ states in ^{56}Mn. The second and third columns are the normalizations obtained by independently adjusting the L=0 and L=2 strengths. The last three columns have the same meaning as in Table IV.

E_x(MeV)	N'(L=0)	N'(L=2)	σ(L=0,θ=0) mb/sr	F(Q)	σ(L=0,θ=0,Q=0) mb/sr
0.11	0.582	1.233	0.23	4.09	0.94±0.19
1.17	0.630	0.477	0.29	4.09	1.20±0.24

Table VI. Results for B(GT) values for 1^+ states in ^{56}Mn from analysis of the ^{56}Fe(^{12}C, ^{12}N)^{56}Mn data and from shell-model calculations.

State	Expt		Theory A[a]		Theory B[b]	Theory C[c]
	E_x(MeV)	B(GT)	E_x(MeV)	B(GT)	B(GT)	B(GT)
1	0.11	0.65±0.17	0.24	0.26	0.88	0.83
2	1.17	0.83±0.22	1.3	2.73	1.23	1.14

[a]Reference 14. The numbers given for E_x and B(GT) do not appear in this form in Ref. 14; they were provided by S.D. Bloom.

[b]Present calculation in the smaller model space described in the text; energy spacing between the two 1^+ levels is 1.26 MeV, compared to 1.06 MeV experimentally.

[c]Present calculation in the larger model space described in the text; energy spacing between the two 1^+ levels is 1.45 MeV, compared to 1.06 MeV experimentally.

FIGURE CAPTIONS

Fig. 1 Spectra for the ($^{12}C, ^{12}N$) and ($^{12}C, ^{12}B$) reactions measured on ^{12}C at E/A = 70 MeV. The angular bin widths are ±0.08°.

Fig. 2 Spectra for $^{26}Mg(^{12}C, ^{12}B)^{26}Al$ at E/A = 70 MeV. The broken arrow indicates the predicted location of the ground state of ^{26}Al. The fourth peak located near 2.8 MeV was used to represent the unidentified strength seen in both the spectra. The angular bin widths are ±0.08°.

Fig. 3 Spectra for $^{54}Fe(^{12}C, ^{12}B)^{54}Co$ at E/A = 70 MeV. The peaks labeled "a" and "b" are at approximately 1.69 and 2.44 MeV excitation, respectively. The angular bin widths are ±0.08°.

Fig. 4 Spectra for $^{58}Ni(^{12}C, ^{12}B)^{58}Cu$ at E/A = 70 MeV. The angular bin widths are ±0.08°.

Fig. 5 Spectra for $^{90}Zr(^{12}C, ^{12}B)^{90}Nb$ at E/A = 70 MeV. The dashed lines show the 5-peak fits described in the text. The position of the peak labeled "a" was allowed to vary. The angular bin widths are ±0.16°.

Fig. 6 Spectra for $^{56}Fe(^{12}C, ^{12}N)^{56}Mn$ at E/A = 70 MeV. The contribution due to the reaction on the H contaminant in the target is shaded. The angular bin widths are ±0.24°.

Fig. 7 Angular distributions for elastic scattering of ^{12}C on ^{90}Zr, ^{54}Fe, and ^{26}Mg at E/A = 70 MeV. The solid curves represent calculations wih the optical potentials of Roussel-Chomaz et al. (Ref. 21). The dashed curves for ^{54}Fe and ^{26}Mg are the predictions with the fitted potentials FE2 and MG2, respectively.

Fig. 8 Angular distributions for various GT transitions plotted versus $q_{\perp}R/R(^{26}Mg)$, where $R/R(^{26}Mg)$ is the sum of the projectile and target radii divided by that of $^{12}C+^{26}Mg$. R was calculated as $r_o(A_p^{1/3} + A_t^{1/3})$, where r_o is a constant that cancels in the ratio $R/R(^{26}Mg)$.

The solid line connects the ^{26}Al points and is to guide the eye only. The ^{56}Mn points are from the (^{12}C, ^{12}N) reaction on ^{56}Fe, all others are from (^{12}C, ^{12}B) reactions.

Fig. 9 Angular distributions for the ^{12}C(^{12}C, ^{12}N)^{12}B(0.0 MeV) and ^{12}C(^{12}C, ^{12}B)^{12}N(0.0 MeV) reactions at E/A = 70 MeV. The curves represent results of DWA calculations described in the text. The solid curve is the full calculation normalized to the (^{12}C, ^{12}N) data; the corresponding L = 0 and L = 2 components are shown by the dashed and long-dashed curves, respectively. The calculation using only the central part of the interaction is shown by the dot-dashed curve.

Fig. 10 Angular distribution for the ^{26}Mg(^{12}C, ^{12}B)^{26}Al(1.06 MeV) reaction at E/A = 70 MeV. The solid and dot-dashed curves represent results of DWA calculations with the Franey-Love and the M3Y interaction, respectively, each separately normalized to the data. The dashed and long-dashed curves are the L=0 and L=2 components of the solid curve.

Fig. 11 Angular distributions for (^{12}C, ^{12}B) reactions at E/A = 70 MeV leading to the indicated 1^+ levels in ^{54}Co, ^{58}Cu and ^{90}Nb. The curves are explained in the text.

Fig. 12 Calculated angular distribution for the ^{26}Mg(^{12}C, ^{12}B)^{26}Al reaction leading to the first 1^+ state in ^{26}Al (solid curve), and the separate contributions from the L_t = 0 and L_t = 2 parts of the transition density in the target system.

Fig. 13 B(GT) values (top) and the ratios of DWA zero-degree cross sections to B(GT) values (bottom) computed from full sd-shell wave functions using the Franey-Love interaction for the six lowest lying 1^+ states in the calculated spectrum of ^{26}Al. The open squares and filled circles denote the ratios for the (L=0 + L=2) and the L=0 cross sections, respectively, and the solid and long-dashed lines are drawn at the average values of these two ratios. The dashed line connects the ratios for the L = 2 parts of the cross sections.

Fig. 14 Transition density (which is a dimensionless quantity as defined in Ref. 26) plotted vs momentum transfer for two of the states populated in $^{26}Mg \rightarrow {}^{26}Al$ transitions. The B(GT) values for the solid and dashed cases are 1.90 and 0.029, respectively.

Fig. 15 Calibration curves determined from the ($^{12}C, {}^{12}B$) reaction on several nuclei at E/A = 70 MeV, as described in the text. The dashed and dot-dashed curves represent a linear and a quadratic fit, respectively.

Fig. 16 Angular distributions for the $^{56}Fe(^{12}C, {}^{12}N)^{56}Mn$ reaction at E/A = 70 MeV, leading to two 1^+ states. The curves represent results of DWA calculations normalized to the data.

Fig. 17 Shell-model result for the T=3 Gamow-Teller strength distribution in ^{56}Mn. The heights of the vertical bars correspond to the calculated B(GT) values. The continuous curve, which is the envelope of these strengths, is obtained by spreading the strength for each state over an energy interval determined by the experimental resolution of 280 keV. The area under each Gaussian is proportional to the corresponding B(GT) value.

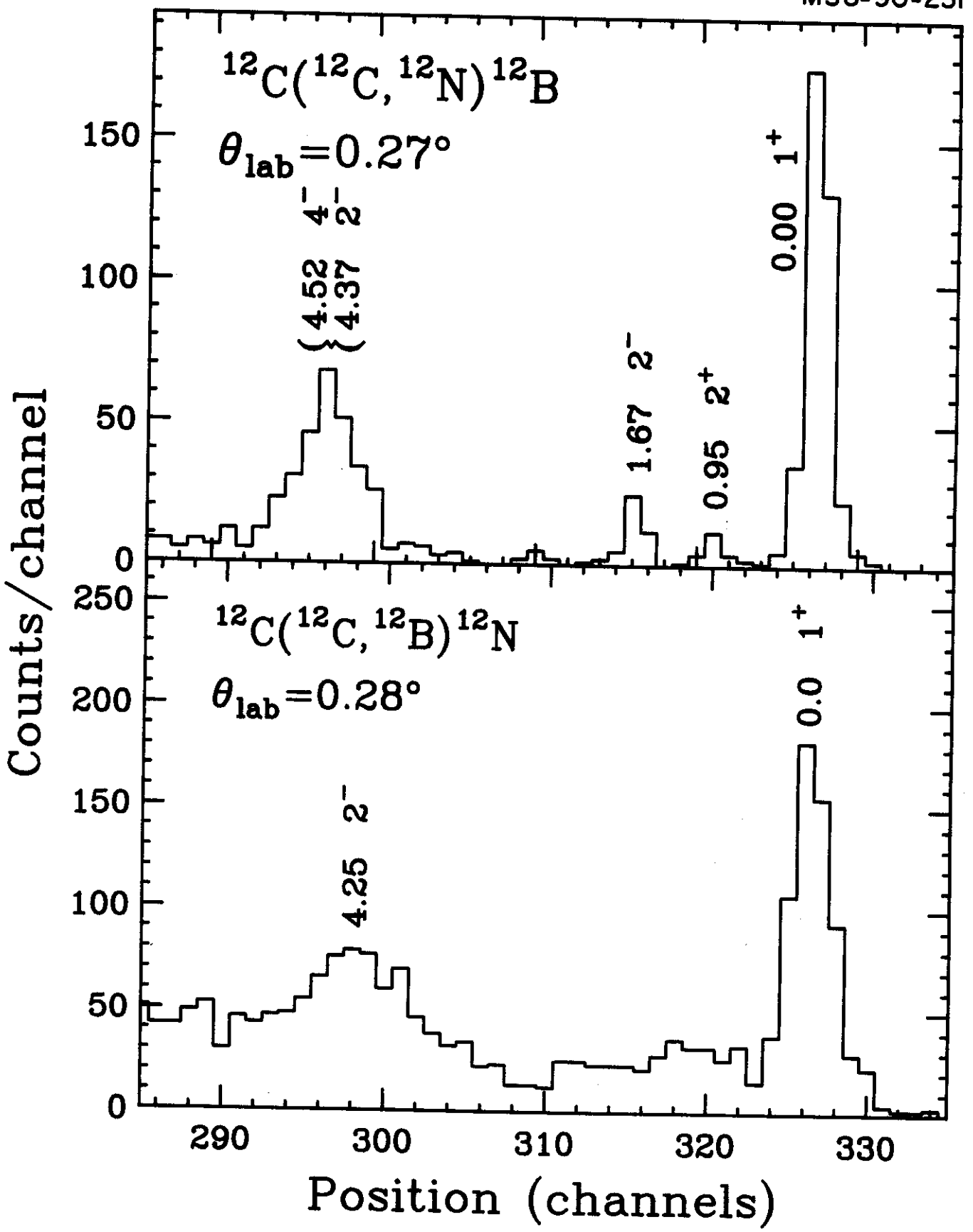
$^{12}C(^{12}C,^{12}N)^{12}B$
$\theta_{lab}=0.27°$
4.52 4⁻
4.37 2⁻
1.67 2⁻
0.95 2⁺
0.00 1⁺
$^{12}C(^{12}C,^{12}B)^{12}N$
$\theta_{lab}=0.28°$
4.25 2⁻
0.0 1⁺
Counts/channel
Position (channels)
0
50
100
150
200
250
290
300
310
320
330

Fig. 1

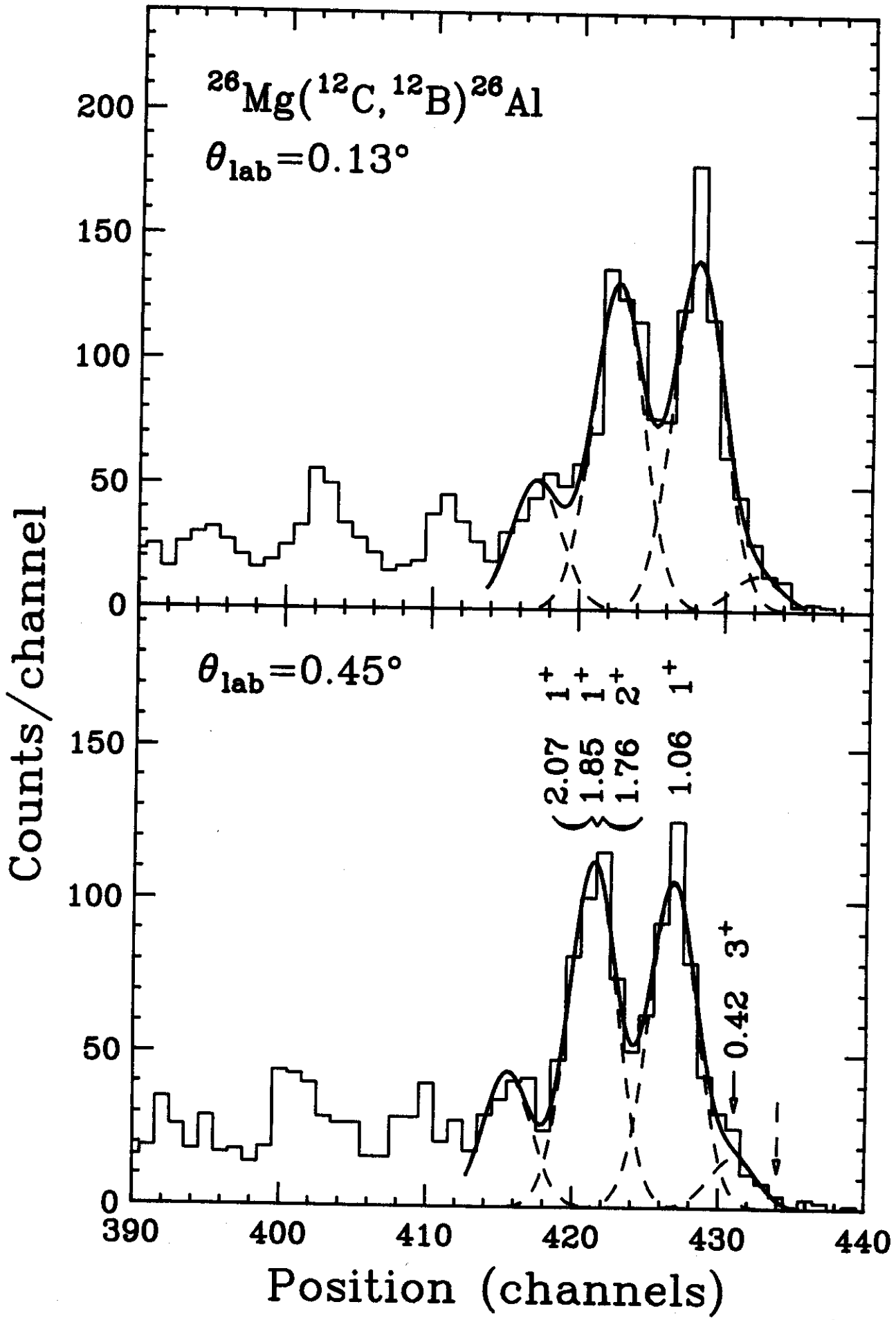
^{26}Mg(^{12}C,^{12}B)^{26}Al
θ_{lab}=0.13°
θ_{lab}=0.45°
1+ 1+ 2+ 1+
2.07 1.85 1.76 1.06
0.42 3+
Counts/channel
Position (channels)
0
50
100
150
200
390
400
410
420
430
440

Fig. 2

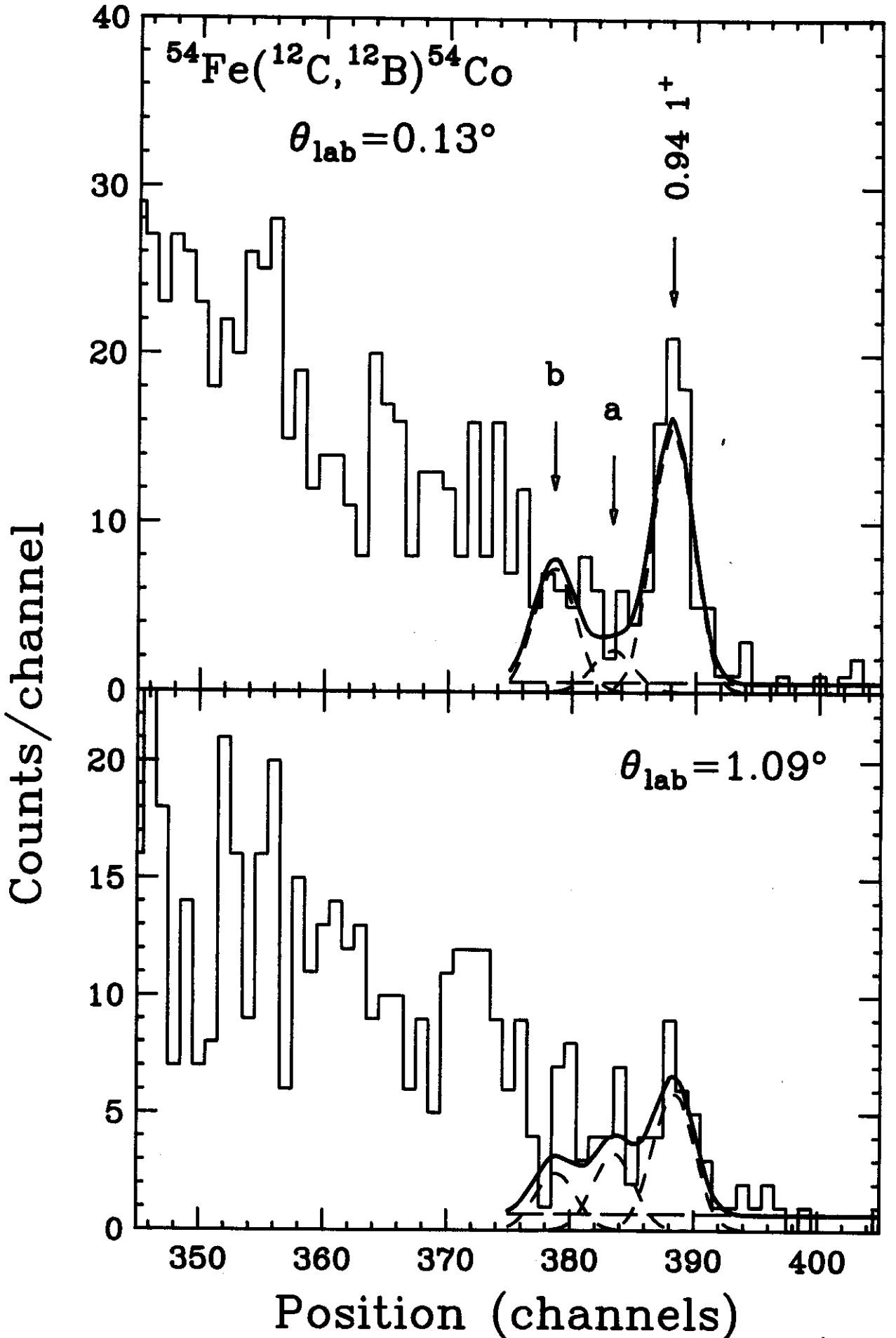
$^{54}Fe(^{12}C,^{12}B)^{54}Co$
θ_{lab}=0.13°
0.94 1+
b
a
θ_{lab}=1.09°
x
Counts/channel
Position (channels)
0
10
20
30
0
5
10
15
20
350
360
370
380
390
400

Fig. 3

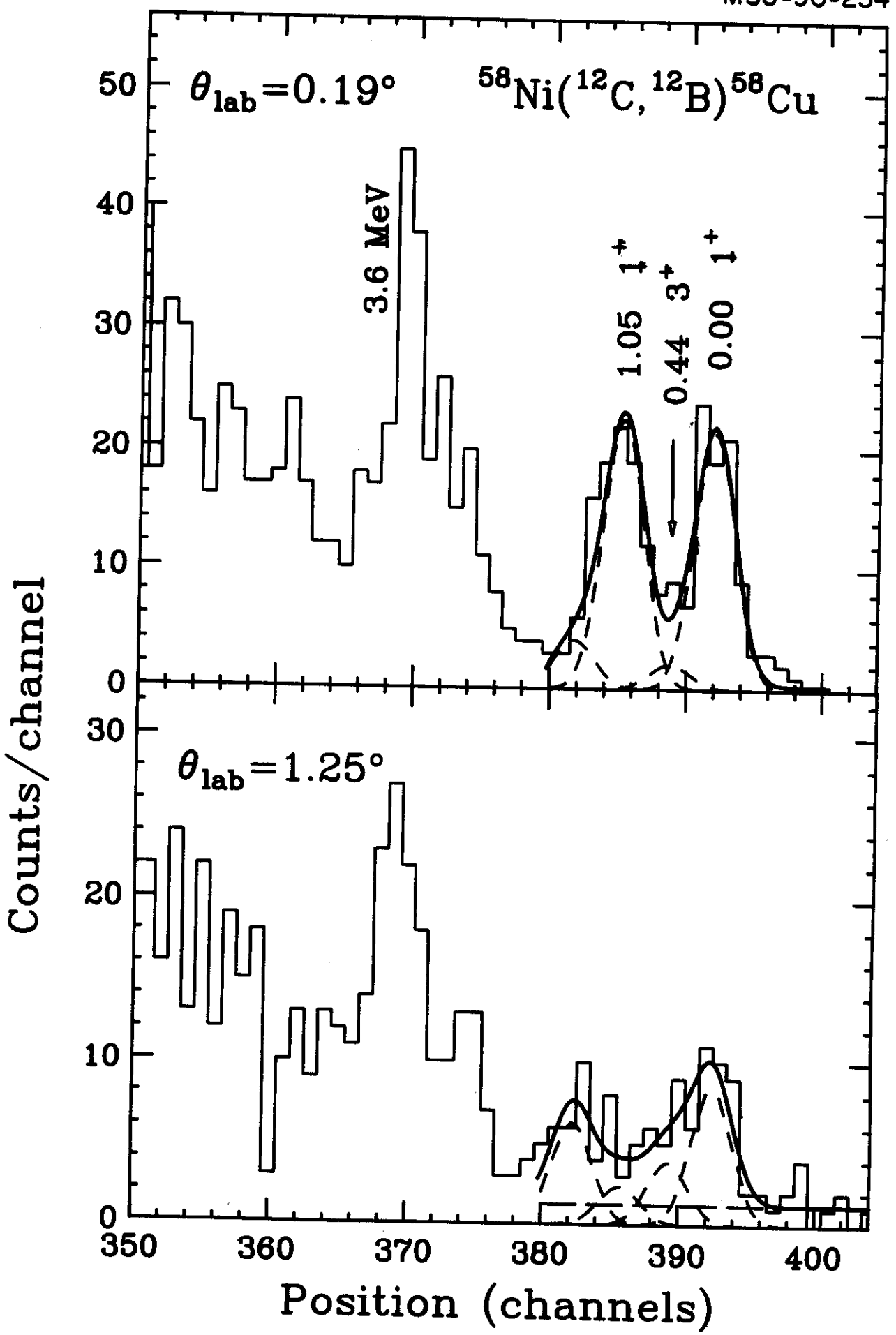
θlab=0.19°
58Ni(12C,12B)58Cu
3.6 MeV
1.05 1+
0.44 3+
0.00 1+
θlab=1.25°
Counts/channel
Position (channels)
0
10
20
30
40
50
350
360
370
380
390
400

Fig. 4

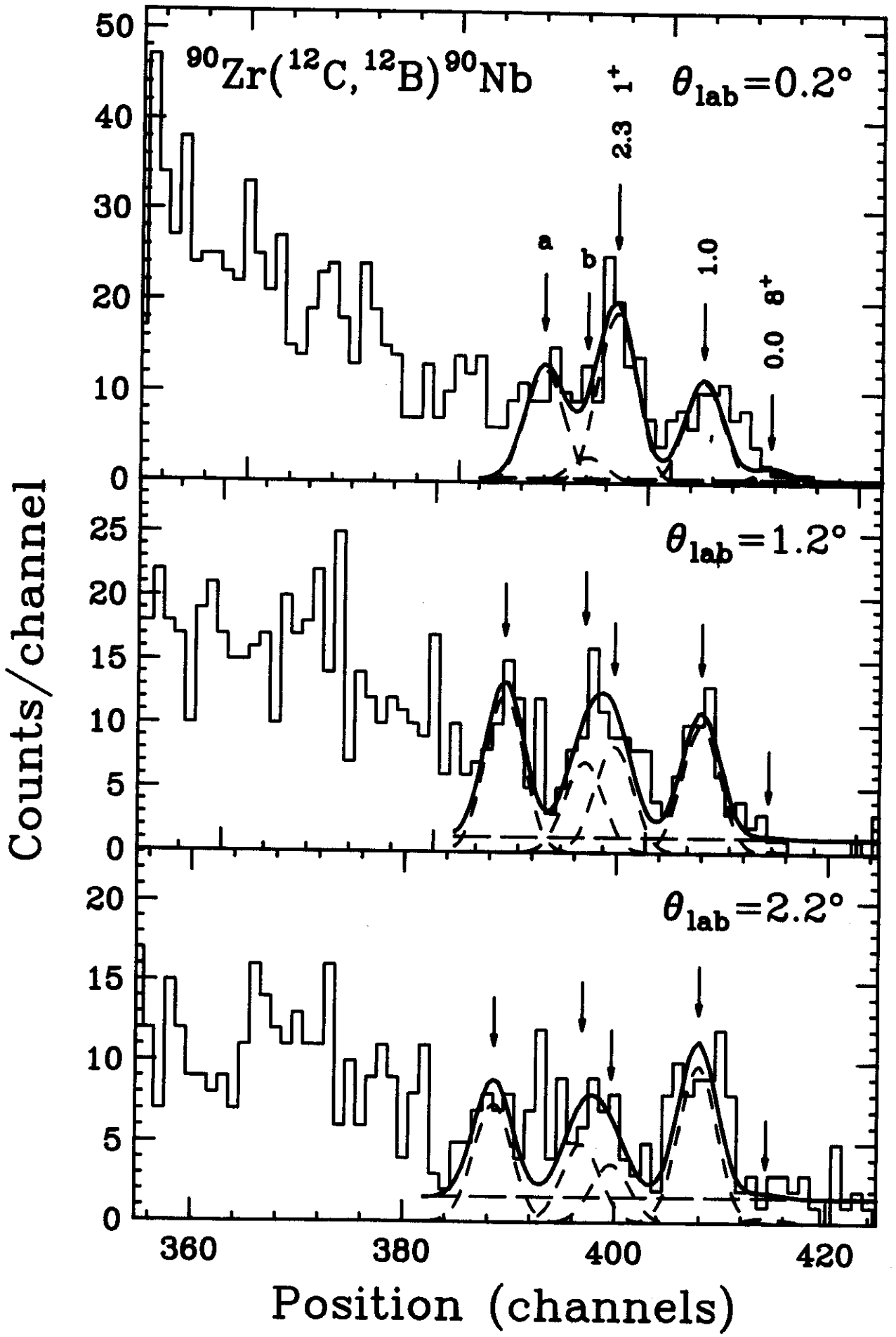
$^{90}Zr(^{12}C,^{12}B)^{90}Nb$
θ_{lab}=0.2°
θ_{lab}=1.2°
θ_{lab}=2.2°
2.3 1+
a
b
1.0
0.0 8+
Counts/channel
Position (channels)
360
380
400
420

Fig. 5

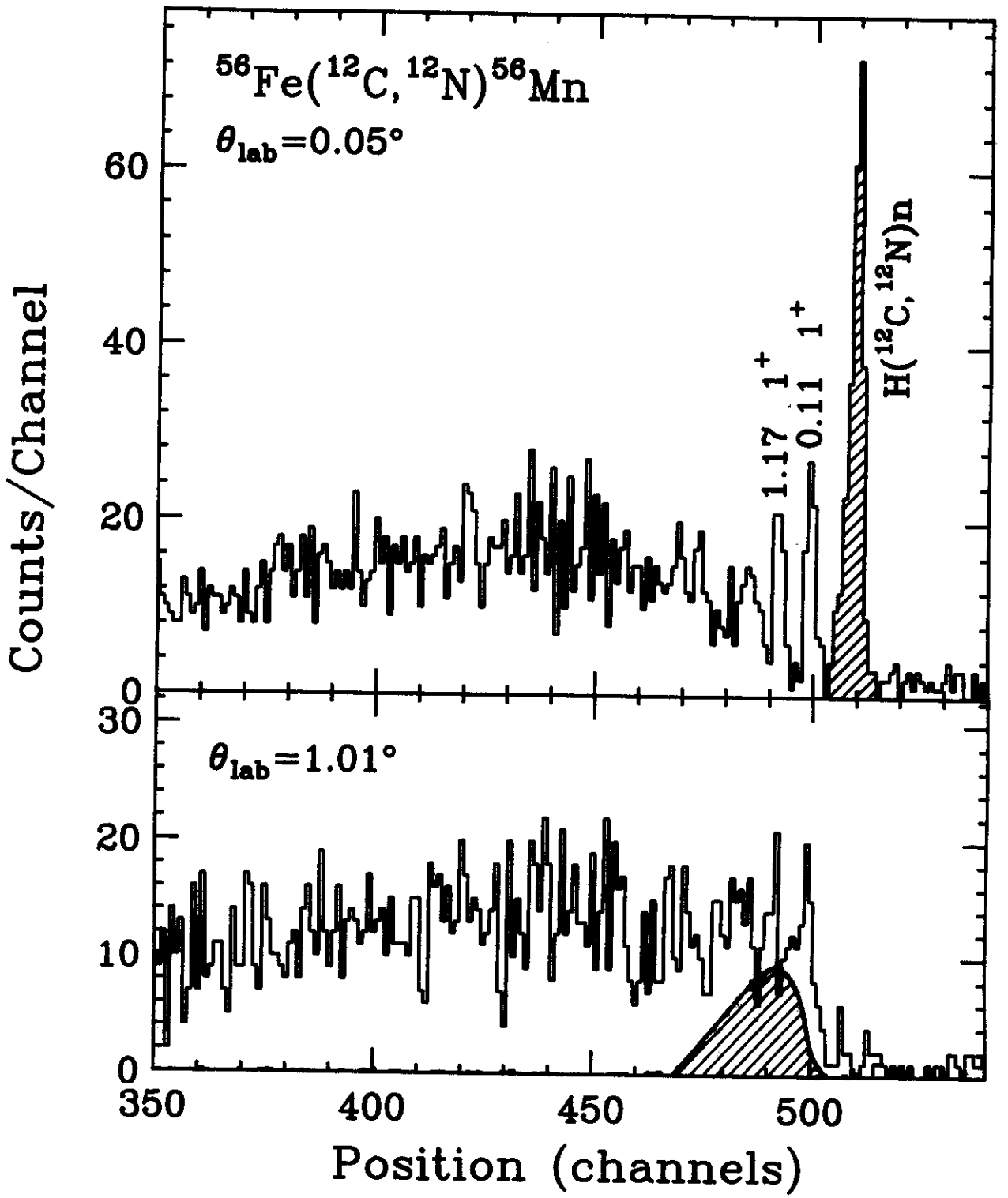
$^{56}Fe(^{12}C,^{12}N)^{56}Mn$
θ_{lab}=0.05°
θ_{lab}=1.01°
1.17 1+
0.11 1+
H(^{12}C,^{12}N)n
Counts/Channel
Position (channels)
0
20
40
60
0
10
20
30
350
400
450
500

Fig. 6

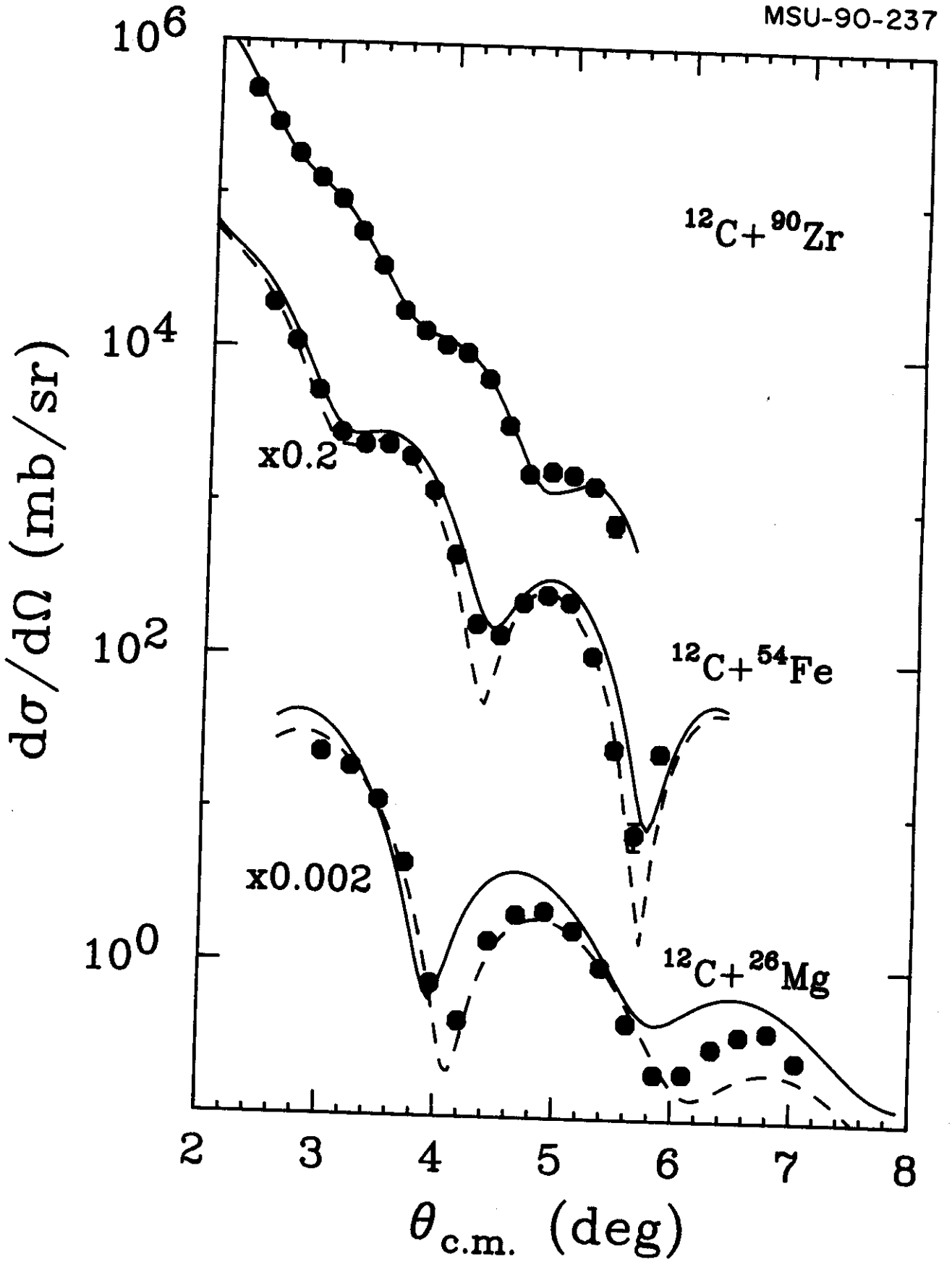
MSU-90-237
10^6
10^4
10^2
10^0
$d\sigma/d\Omega$ (mb/sr)
$^{12}C+^{90}Zr$
x0.2
$^{12}C+^{54}Fe$
x0.002
$^{12}C+^{26}Mg$
2
3
4
5
6
7
8
$\theta_{c.m.}$ (deg)

Fig. 7

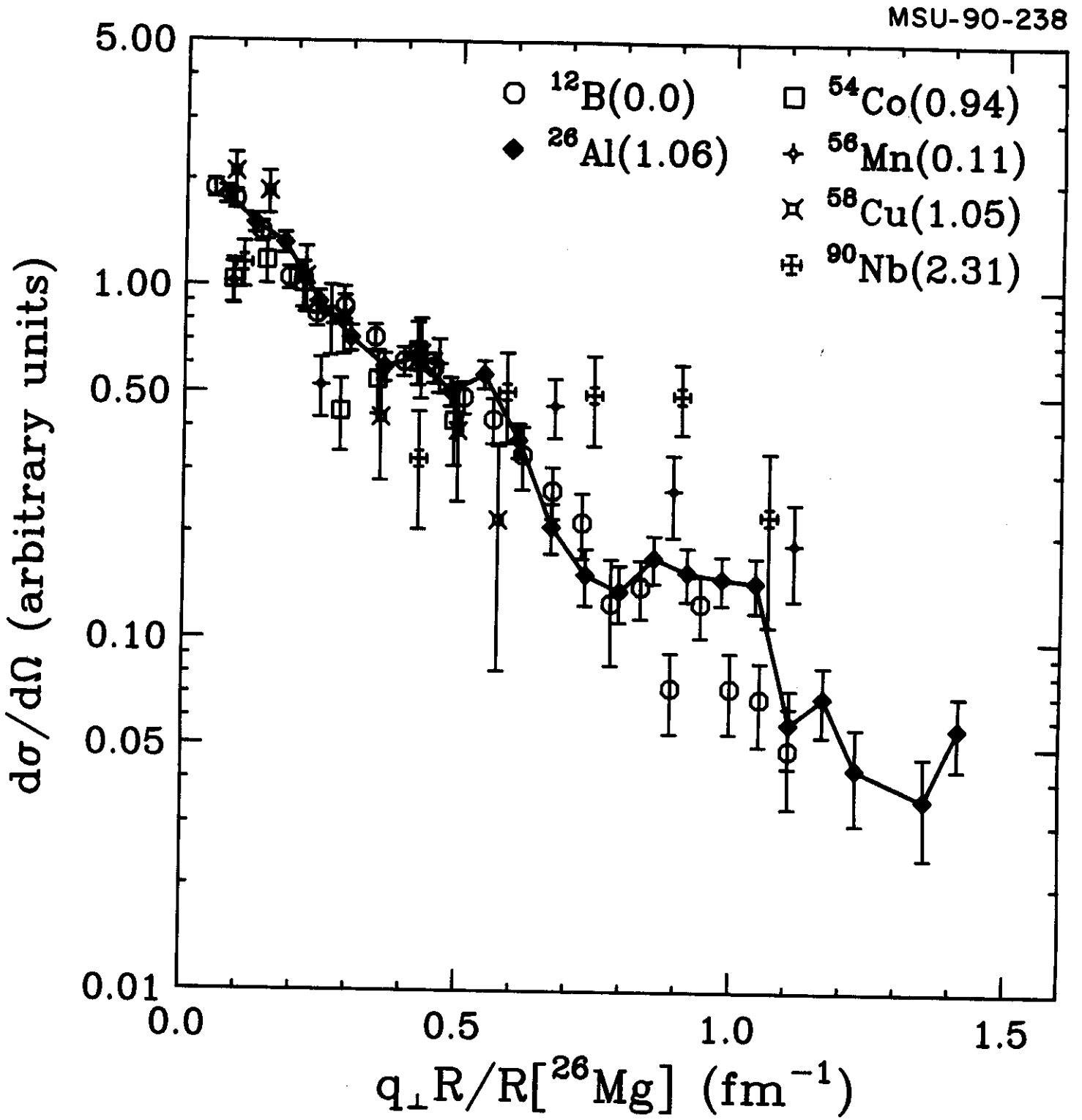
MSU-90-238
5.00
1.00
0.50
0.10
0.05
0.01
0.0
0.5
1.0
1.5
dσ/dΩ (arbitrary units)
q⊥R/R[26Mg] (fm−1)
12B(0.0)
26Al(1.06)
54Co(0.94)
56Mn(0.11)
58Cu(1.05)
90Nb(2.31)

Fig. 8

MSU-90-239

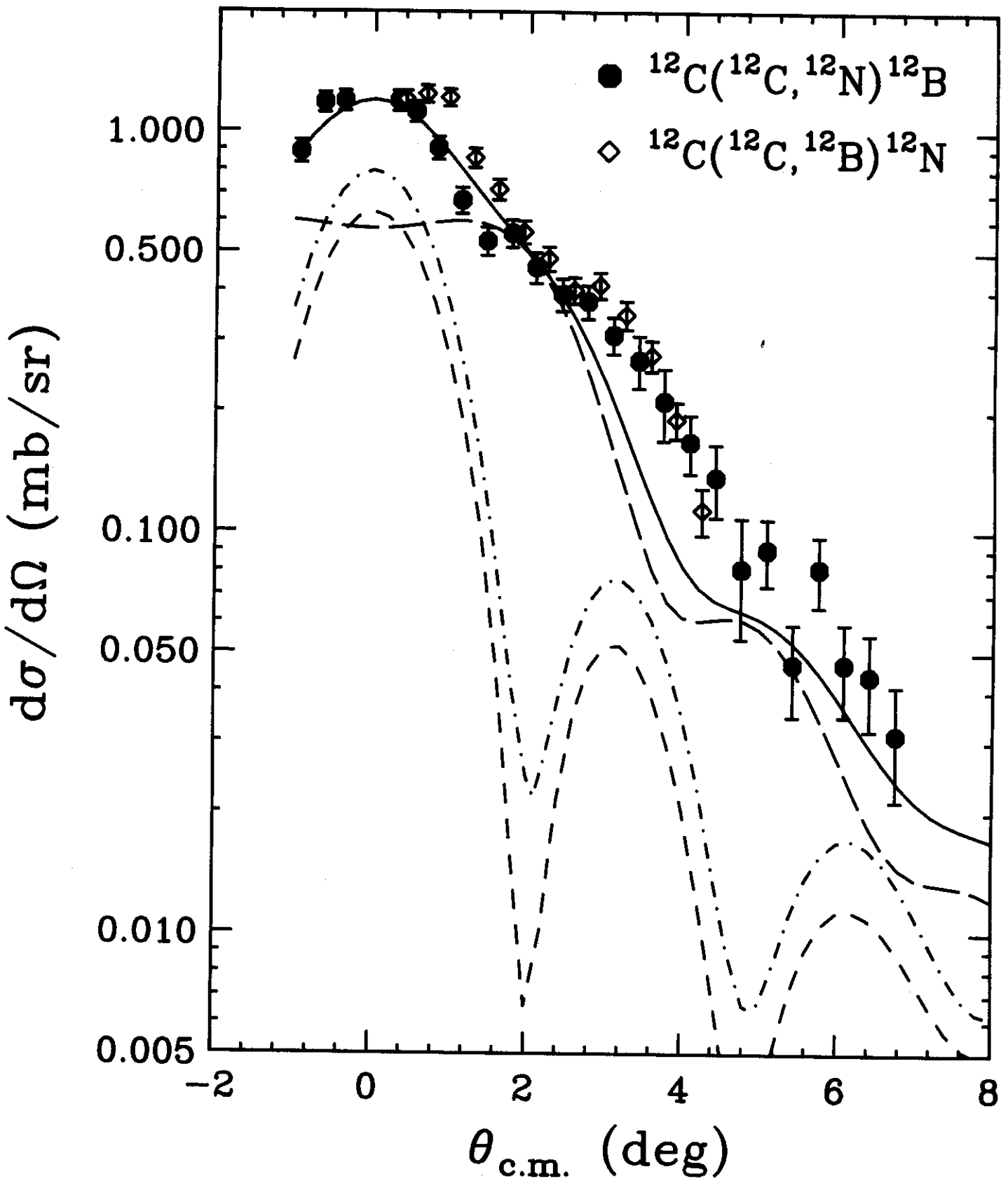

Fig. 9

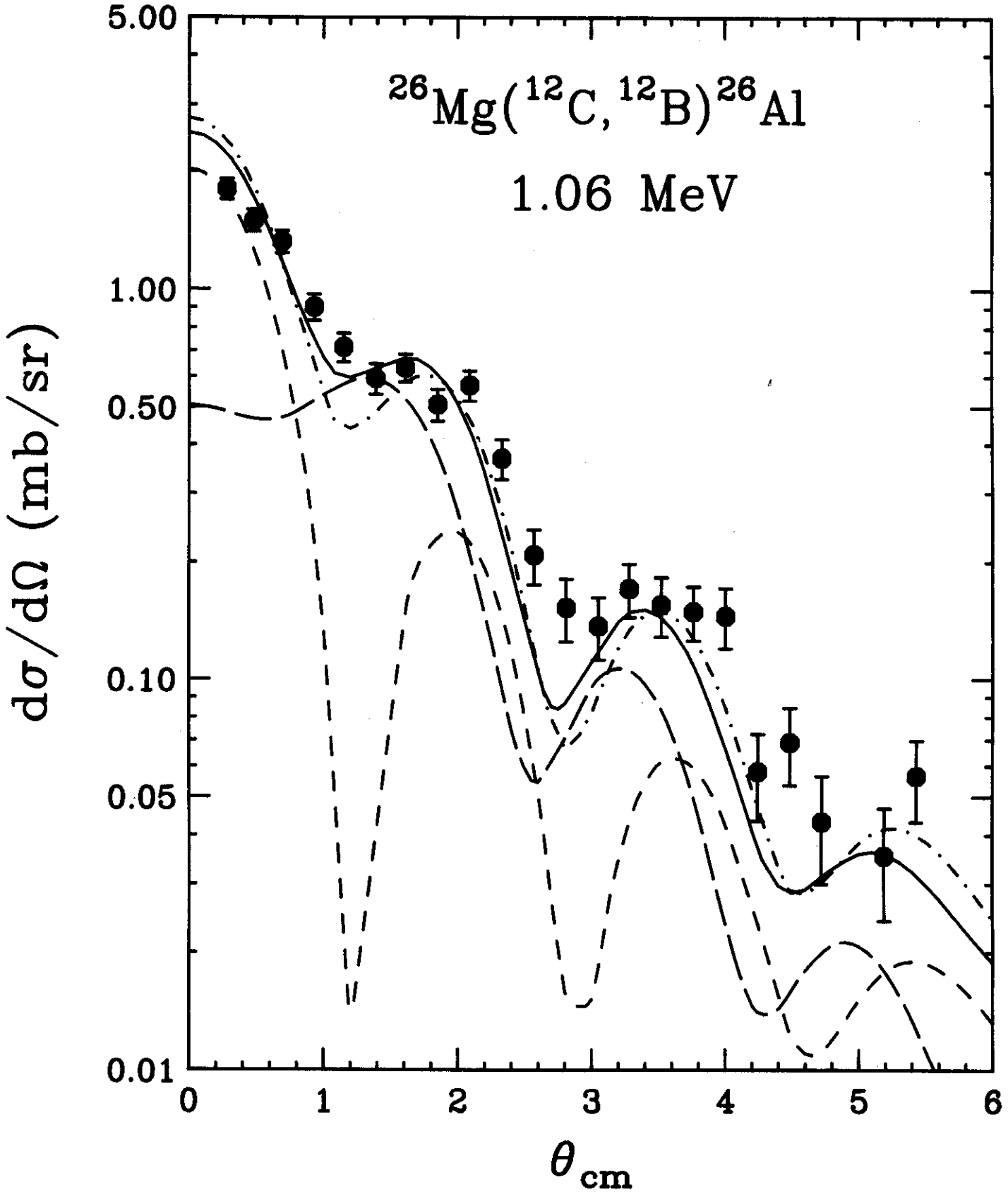
$^{26}Mg(^{12}C,^{12}B)^{26}Al$
1.06 MeV
dσ/dΩ (mb/sr)
5.00
1.00
0.50
0.10
0.05
0.01
0
1
2
3
4
5
6
θcm

Fig. 10

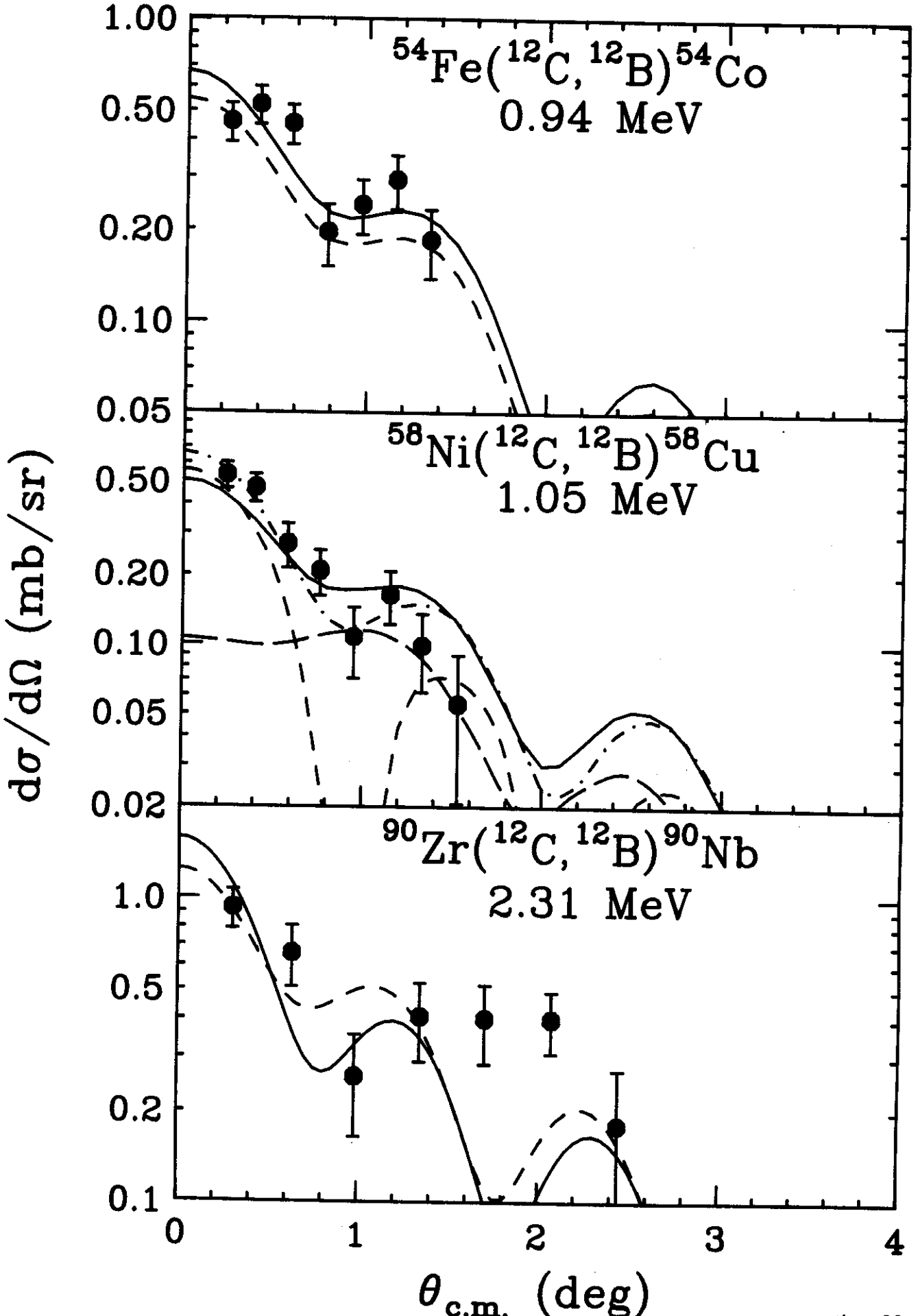
^{54}Fe(^{12}C,^{12}B)^{54}Co
0.94 MeV
^{58}Ni(^{12}C,^{12}B)^{58}Cu
1.05 MeV
^{90}Zr(^{12}C,^{12}B)^{90}Nb
2.31 MeV
dσ/dΩ (mb/sr)
θc.m. (deg)
1.00
0.50
0.20
0.10
0.05
0.02
1.0
0.5
0.2
0.1
0
1
2
3
4

Fig. 11

MSU-90-242

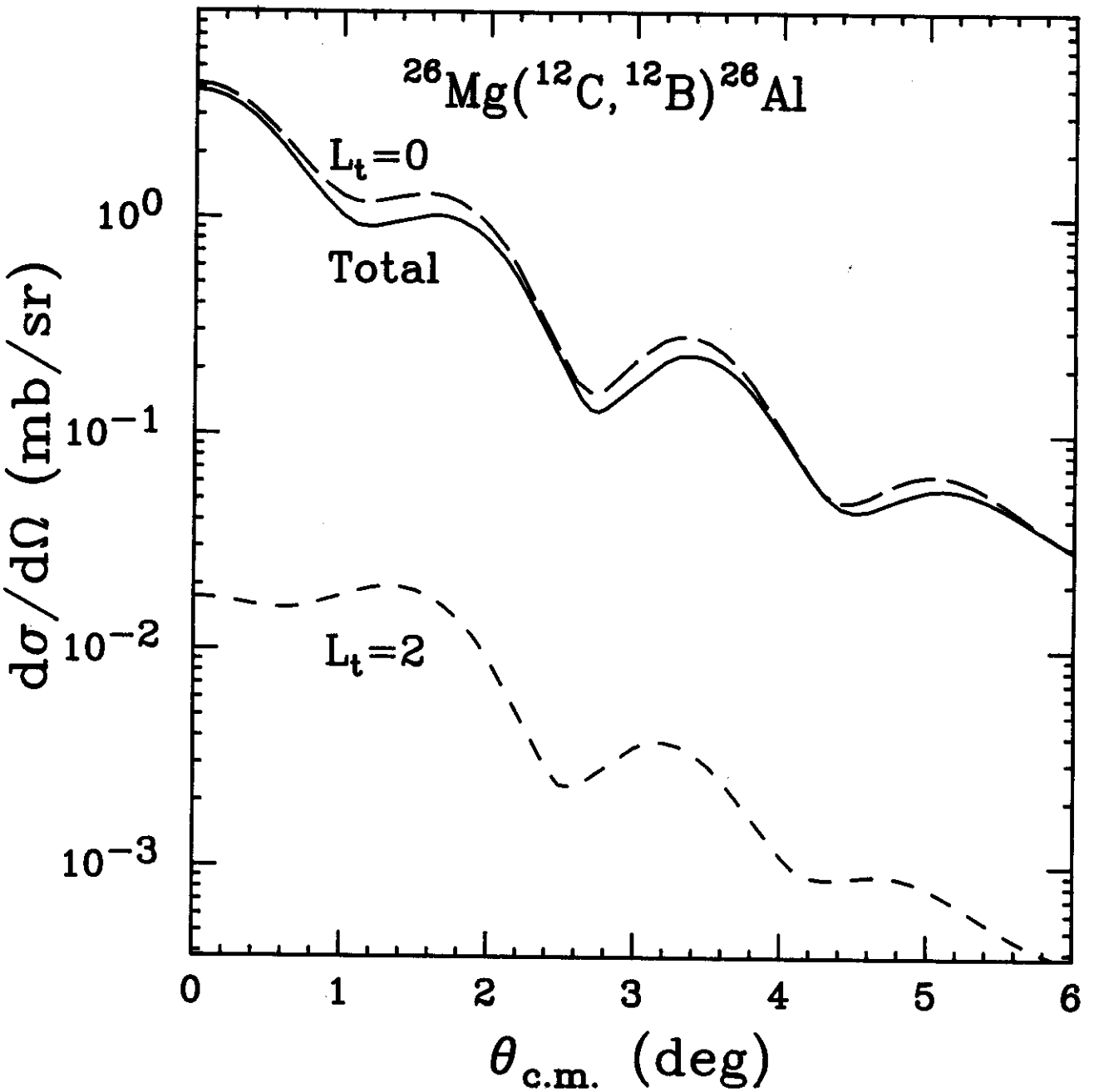

Fig. 12

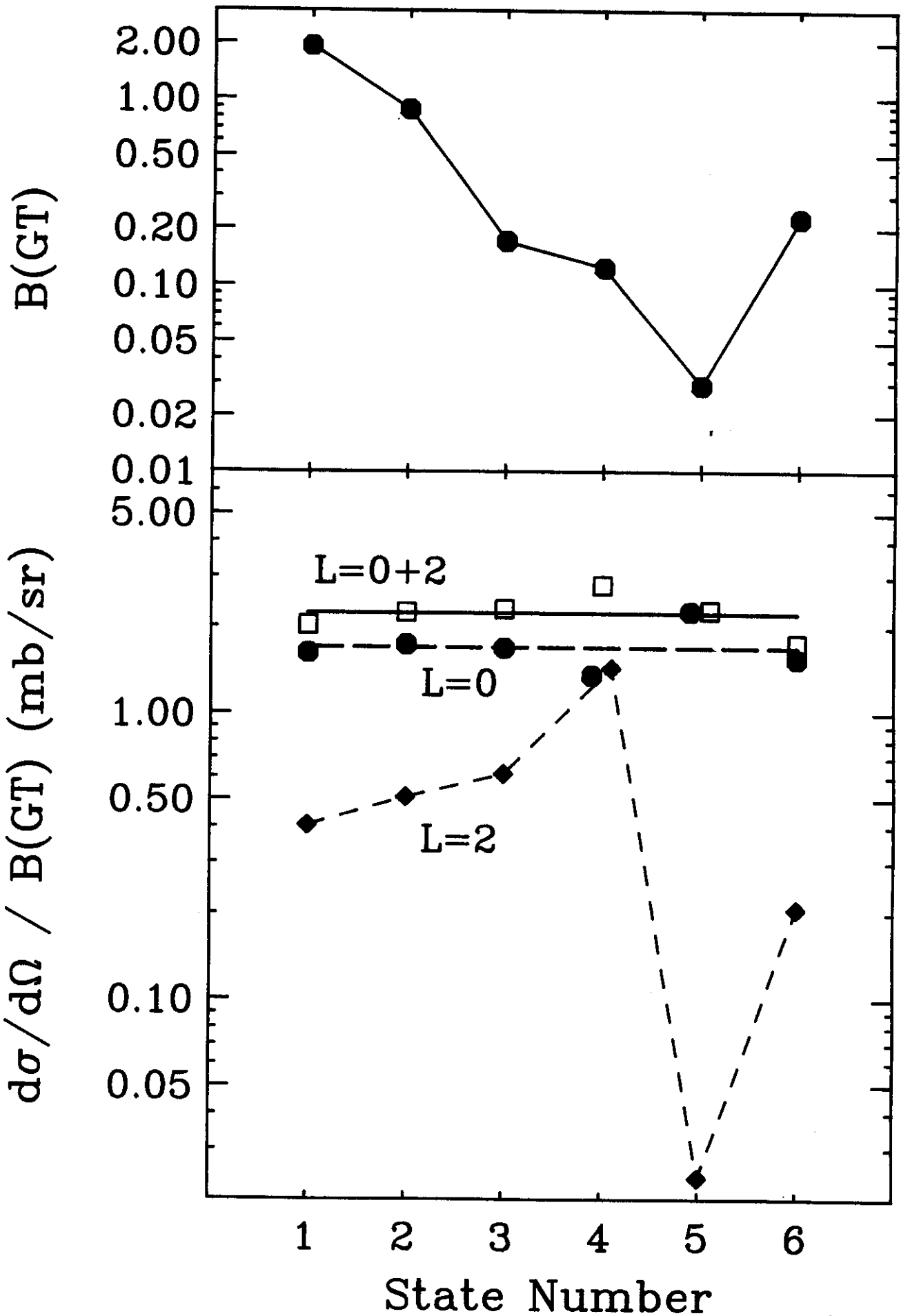
B(GT)
2.00
1.00
0.50
0.20
0.10
0.05
0.02
0.01
dσ/dΩ / B(GT) (mb/sr)
5.00
1.00
0.50
0.10
0.05
L=0+2
L=0
L=2
1
2
3
4
5
6
State Number

Fig. 13

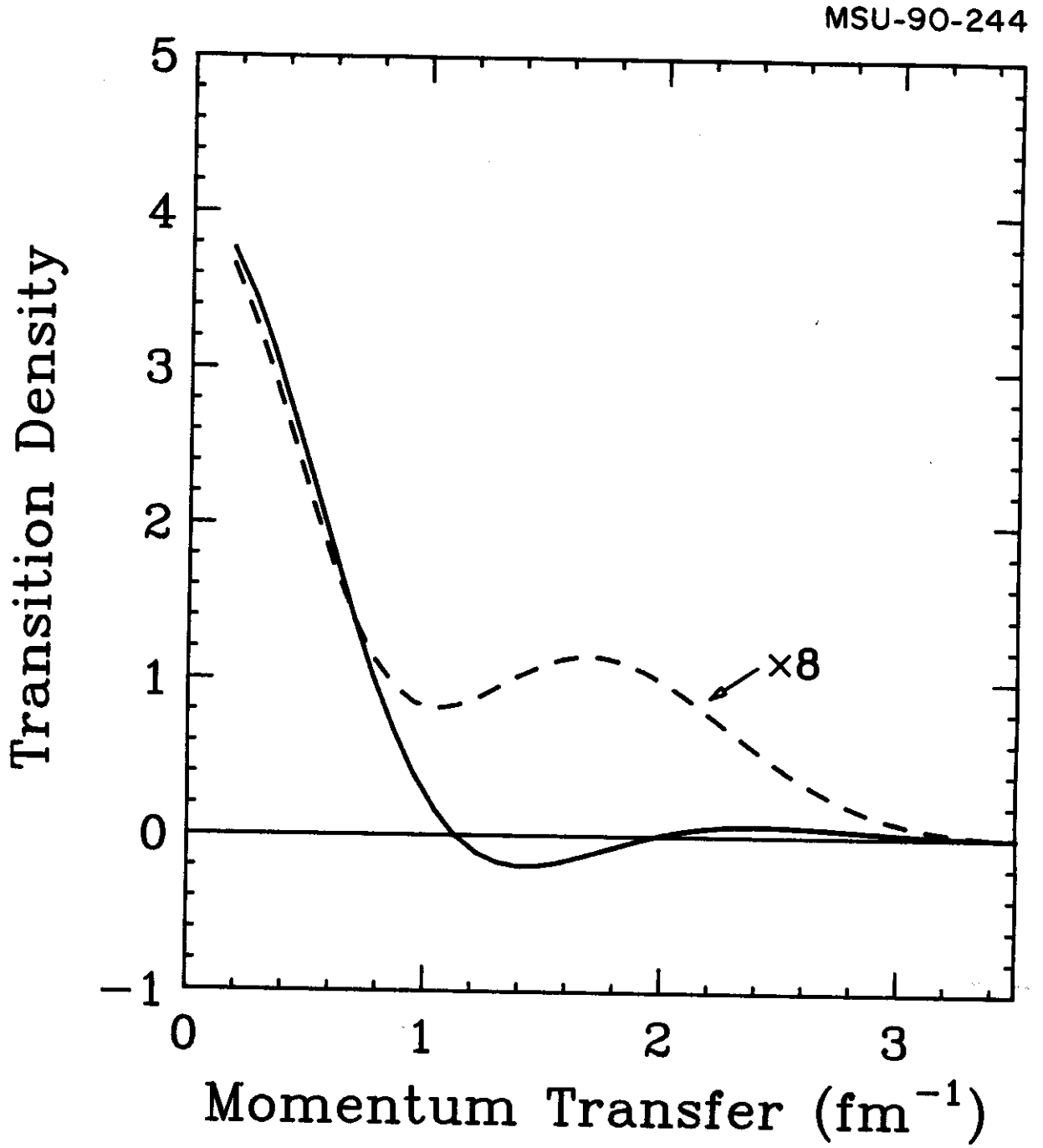
MSU-90-244
Transition Density
5
4
3
2
1
0
−1
0
1
2
3
Momentum Transfer (fm^{-1})
×8

Fig. 14

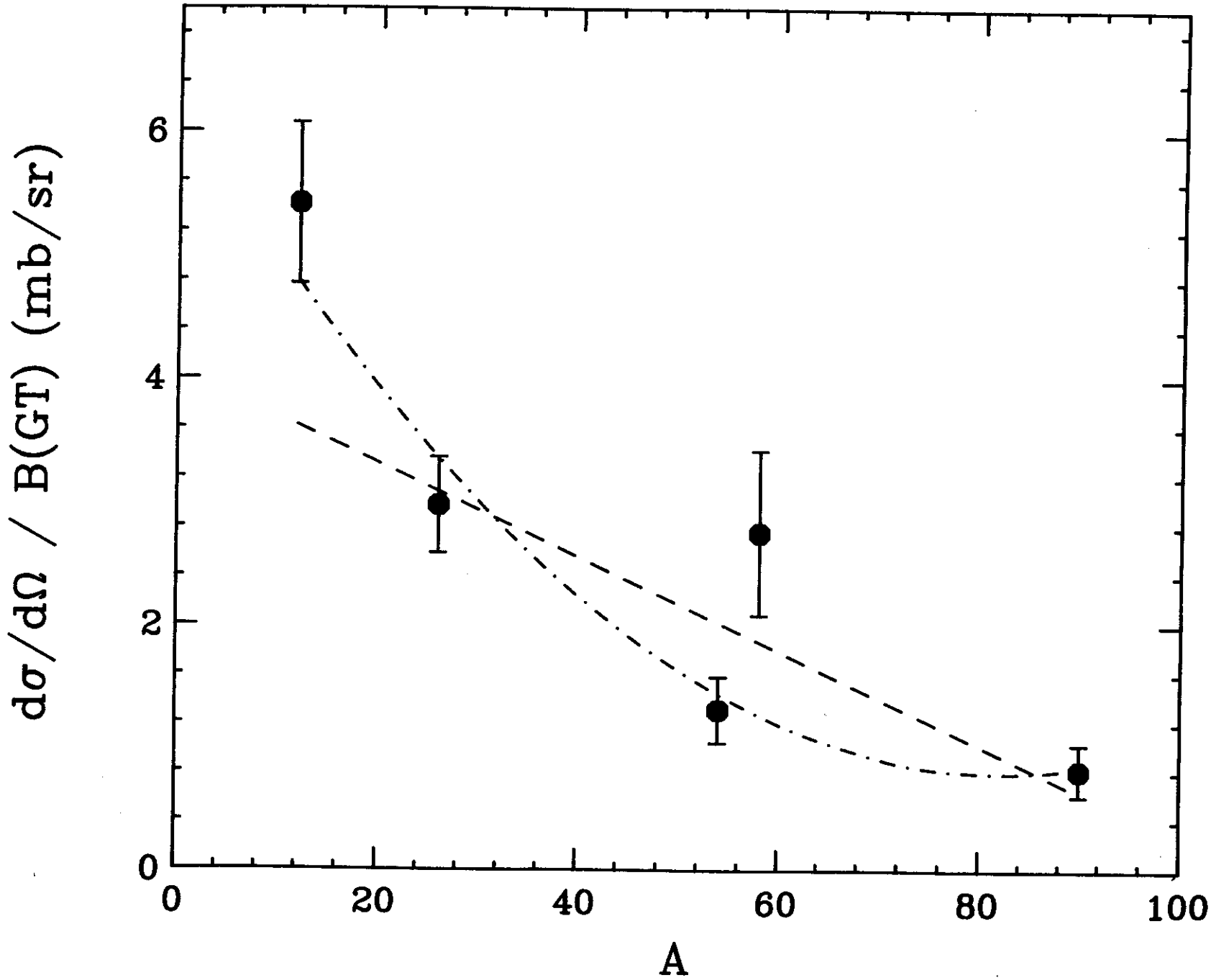

Fig. 15

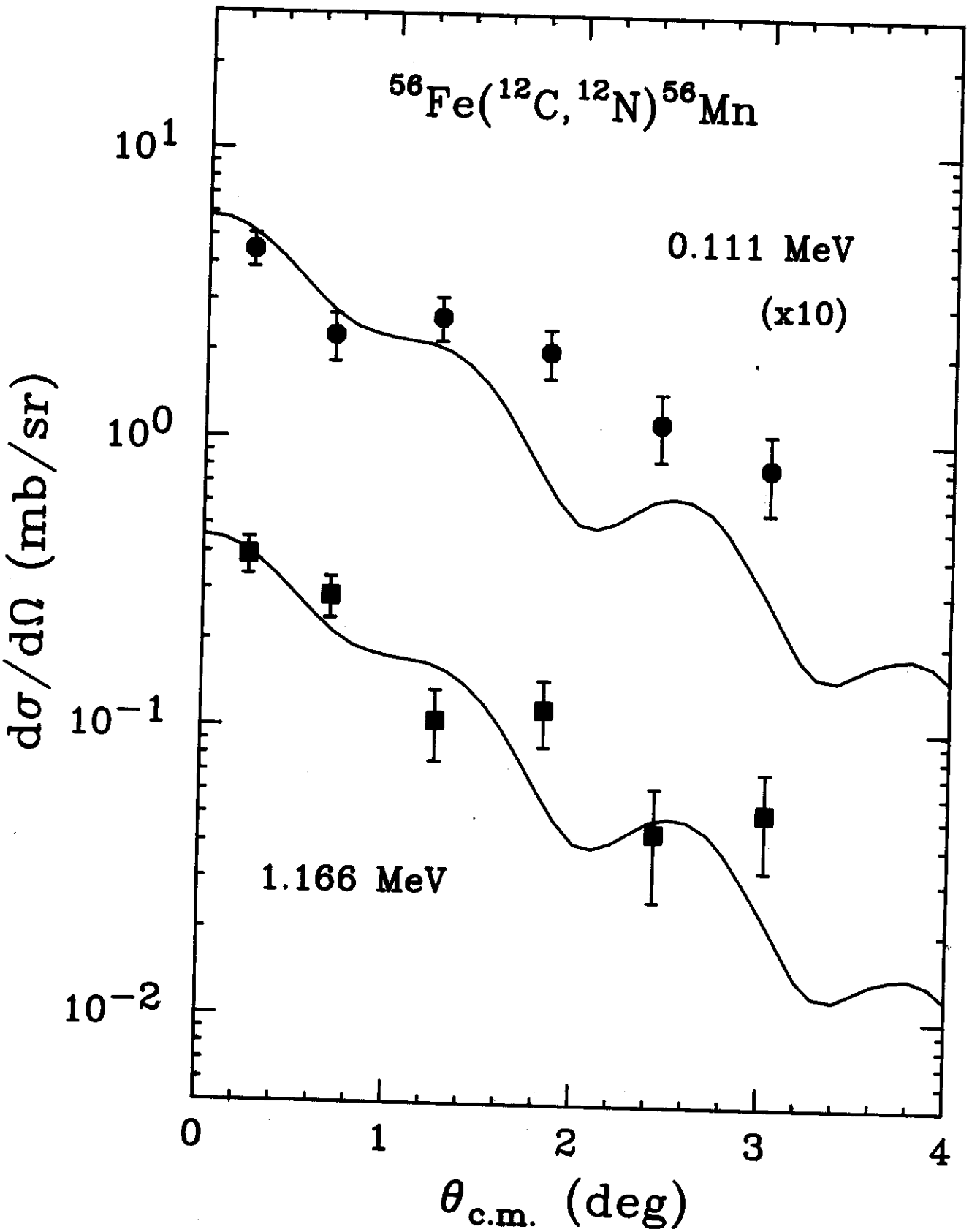
$^{56}Fe(^{12}C,^{12}N)^{56}Mn$
0.111 MeV
(x10)
1.166 MeV
$d\sigma/d\Omega$ (mb/sr)
10^1
10^0
10^{-1}
10^{-2}
0
1
2
3
4
$\theta_{c.m.}$ (deg)

Fig. 16

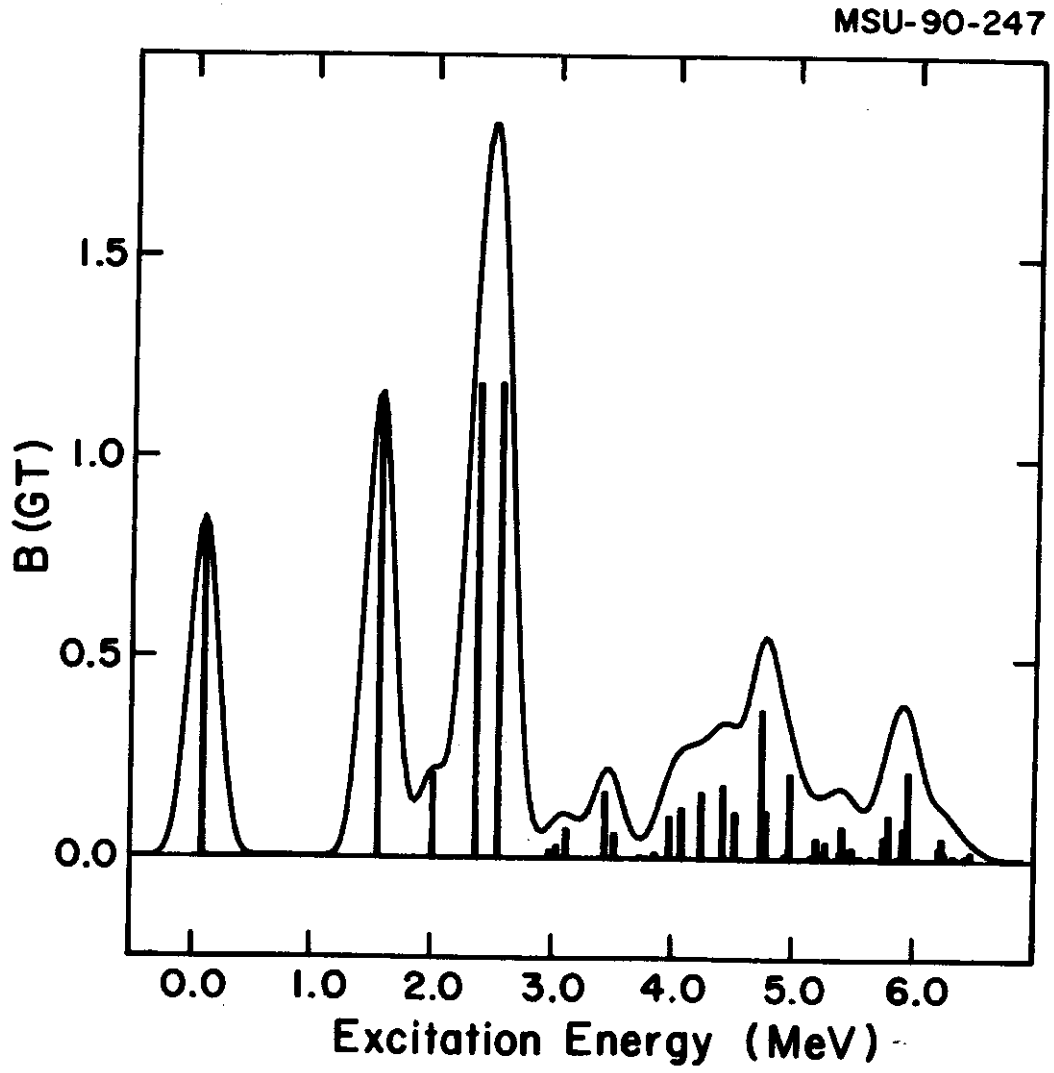
MSU-90-247
B(GT)
1.5
1.0
0.5
0.0
0.0
1.0
2.0
3.0
4.0
5.0
6.0
Excitation Energy (MeV)

Fig. 17